

Distinguishing Tidal Disruption Events and Changing-look Active Galactic Nuclei via Variation of Mid-infrared Color

YUJUN YAO,¹ JINGJING YE,¹ LUMING SUN,¹ NING JIANG,^{2,3} MEGAN MASTERSON,⁴ AND XINWEN SHU¹

¹*Department of Physics, Anhui Normal University, Wuhu, Anhui 241002, China*

²*CAS Key Laboratory for Researches in Galaxies and Cosmology, Department of Astronomy, University of Science and Technology of China, Hefei, Anhui 230026, China*

³*School of Astronomy and Space Sciences, University of Science and Technology of China, Hefei, 230026, China*

⁴*MIT Kavli Institute for Astrophysics and Space Research, Massachusetts Institute of Technology, Cambridge, MA 02139, USA*

ABSTRACT

At present, there is a lack of effective probes to distinguish between mid-infrared (MIR) outbursts induced by tidal disruption events (TDEs) and changing-look active galactic nuclei (CLAGNs) based on only MIR data. Here, we propose that the time variation of MIR color is a promising probe. With an optically selected sample containing TDEs, ambiguous nuclear transients (ANTs), and CLAGNs, we studied the variation of MIR color after subtracting the quiescent fluxes using NEOWISE-R data. We found that the MIR color of TDEs and ANTs turns red faster than CLAGNs during the rising phase, and TDEs have a redder color than ANTs at the earliest phase. The former may be caused by the difference between the ultraviolet light curves of TDEs/ANTs and CLAGNs, or be related to no or weak underlying AGN in TDEs/ANTs, while the latter may be related to the difference in the dust geometry. Based on color variation rate, we selected high-probability TDE, ANT, and CLAGN candidates from MIR outbursts in samples of Jiang et al. (2021) and Masterson et al. (2024). We found that both samples are mixtures of TDEs/ANTs and CLAGNs. For MIR outbursts whose hosts are not Seyfert galaxies, we estimated that $\sim 50\% - 80\%$ are TDEs and inferred a rate of infrared TDEs of $1.5 - 2.8 \times 10^{-5} \text{ galaxy}^{-1} \text{ yr}^{-1}$, comparable with that of optical TDEs. The rest are CLAGNs, suggesting the presence of weak AGNs that cannot be identified using common diagnoses. Our work opens a new door for future classification of infrared selected transients.

1. INTRODUCTION

In quiescent galaxies, which account for the majority of galaxies, tidal disruption events (TDEs) are powerful probes of supermassive black holes (SMBHs). A TDE occurs when a star wanders too close to the SMBH for its own gravity to resist the tidal force (e.g., Rees 1988). TDEs can be observed through bright flares lasting for months to years (e.g., van Velzen et al. 2020). Thanks to the development of time-domain surveys, $\gtrsim 100$ TDEs have been discovered. Most of TDEs are selected in the optical band (optical TDEs) via their bright UV-optical emission (e.g., van Velzen et al. 2020; Hammerstein et al. 2023), while a small number are selected in the X-ray band (X-ray TDEs) via their bright X-ray emission (e.g., Saxton et al. 2020; Sazonov et al. 2021), and some are bright in both bands (e.g., Guolo et al. 2024). Ac-

ording to recent sample studies, the incidence rate of optical TDEs is around $3 \times 10^{-5} \text{ galaxy}^{-1} \text{ yr}^{-1}$ (e.g., Yao et al. 2023), while that of X-ray TDEs is around $1 \times 10^{-5} \text{ galaxy}^{-1} \text{ yr}^{-1}$ (e.g., Sazonov et al. 2021). In addition, the TDE rate is related to the properties of the host galaxy. For example, post-starburst galaxies have a higher incidence rate of TDEs than normal galaxies (e.g., French et al. 2016; Yao et al. 2023).

Despite these findings, there is a lack of complete TDE samples because dust-obscured TDEs are hard to detect by optical or X-ray surveys. Fortunately, the TDE's UV emission heats the surrounding dust to produce infrared (IR) re-radiation, known as IR echo (e.g., Jiang et al. 2016; van Velzen et al. 2016). Dust-obscured TDEs can reveal themselves by their IR echoes as IR outbursts, for example, Arp 299-B AT1 (Mattila et al. 2018) and AT 2017gbl (Kool et al. 2020). Thanks to the all-sky mid-infrared (MIR) sky survey of the Wide-field Infrared Survey Explorer (WISE, Wright et al. 2010), hundreds of MIR outbursts in centers of galaxies have been discov-

ered (Jiang et al. 2021; Reynolds et al. 2022; Masterson et al. 2024; Necker et al. 2024). The derived event rate is $\sim 2 - 5 \times 10^{-5}$ galaxy $^{-1}$ yr $^{-1}$, similar to the rate of optical and X-ray TDEs, implying that optical and X-ray surveys may have missed a significant fraction of TDEs.

However, a key question remains unanswered: are these MIR outbursts TDEs? Although the authors of previously mentioned works preferred that their samples consist mainly of obscured TDEs, there is doubt (e.g., Dodd et al. 2023) that changing-look active galactic nuclei (CLAGN) contribute to these MIR outbursts significantly. CLAGNs (see review in Ricci & Trakhtenbrot 2023) can also produce MIR outbursts (e.g., Sheng et al. 2017; Lyu et al. 2022). Despite many differences between TDEs and CLAGNs in UV/optical bands in terms of light curves (LCs) and spectra (e.g., Zabludoff et al. 2021), distinguishing their IR echoes remains challenging. Differences in the UV/optical LCs are blurred by the light travel time effect of the echo, and the spectral features that may distinguishing the two are lost when the emission is reprocessed to the IR band. To make matters worse, there is a class of outbursts in active galactic nuclei (AGN) that share the characteristics of both TDEs and CLAGNs, for example AT 2016ezh (=PS16dtm, Blanchard et al. 2017; Petrushevska et al. 2023), AT 2017bgt (Trakhtenbrot et al. 2019), AT 2018bcb (=ASASSN-18jd, Neustadt et al. 2020), and some others. These outbursts are referred to as ambiguous nuclear transients (ANTs) as their natures are difficult to determine through UV/optical information: they may be TDEs that occur in AGNs (e.g., Blanchard et al. 2017), or enhanced accretions onto SMBHs (e.g., Trakhtenbrot et al. 2019). In any case, it is almost impossible to distinguish using MIR information only. The nature of MIR outbursts can be distinguished by radio jet (e.g. for Arp 299-B AT1, Mattila et al. 2018), broad emission lines in the near-infrared (NIR) spectra (e.g. for AT 2017gbl, Kool et al. 2020) or optical spectra (e.g., Wang et al. 2022a), or shape of X-ray spectrum (e.g., Masterson et al. 2024). However, these data are not available for the vast majority of MIR outbursts. Therefore, there needs to be an effective probe to distinguish between TDEs and CLAGNs based on only MIR data.

Jiang et al. (2017) noticed that the dust temperature in AT 2016ezh was high with a blackbody temperature $T_{\text{BB}} \gtrsim 2,000$ K initially, and then rapidly dropped to $T_{\text{BB}} \sim 1,000$ K in 100–300 days. Although the temperature values here may not be accurate because the dust properties are uncertain, the trend of temperature decline is robust. Similar rapid drops in dust temperatures

have also been observed in other TDEs, ANTs and TDE candidates (e.g., Mattila et al. 2018; Sun et al. 2020; Kool et al. 2020; Reynolds et al. 2022; Hinkle 2024). However, such drops were not found in CLAGNs¹. We guessed that there may be a general difference in the time variation of dust temperature between TDEs and CLAGNs. The primary purpose of this work is to verify this difference and attempt to distinguish TDEs from CLAGNs using this difference.

This paper is organized as follows. We collected optically selected outbursts, generated MIR LCs and selected those with strong IR echoes in section 2. We studied the MIR color variation and proposed a new method for distinguishing TDEs and CLAGNs in section 3. We applied the method to MIR outburst samples and selected promising TDE and CLAGN candidates in section 4. We discuss in section 5 and summarize and conclude in section 6. Throughout this paper, we used cosmological parameters of $H_0 = 70$ km s $^{-1}$ Mpc $^{-1}$, $\Omega_m = 0.3$ and $\Omega_\Gamma = 0.7$.

2. OPTICALLY-SELECTED OUTBURSTS AND DATA REDUCTION

In order to study the variation of MIR colors of TDEs, CLAGNs and ANTs, and to check the disparity between different types, we collected outbursts whose type can be defined by optical observations. Although in the literature, the term ANT was also used by some authors to refer to different meanings, we will strictly use the term to mean the transient source occurring in an AGN whose nature is being debated. We required the outburst to have a bright MIR emission, and the variation of MIR color in its rising phase can be studied. The requirements and final samples are described in detail in sections 2.1 to 2.3, and the MIR properties of the sample are displayed in section 2.4.

2.1. MIR-bright TDEs, CLAGNs and ANTs

We collected optical TDEs from the ZTF sample (van Velzen et al. 2021; Hammerstein et al. 2023; Yao et al. 2023) and other literature. We applied a redshift cut of $z < 0.35$, the same as Jiang et al. (2021). The NEOWISE-R project (Mainzer et al. 2014) provides the MIR data of all the objects in the W1 and W2 bands (central wavelengths 3.35 and 4.60 μm) between its start in December 2013 and the WISE telescope’s retirement in July 2024. We obtained the MIR

¹ Although some works claimed a “redder when brighter” trend in MIR emission of CLAGNs (Yang et al. 2018), they did not subtract the host galaxy’s contribution to IR emission when they calculated the color

LCs in the W1 and W2 bands sampled every half a year following Jiang et al. (2021). In summary, we queried single-exposure photometries requiring separation of less than 3 arcsecs using NASA/IPAC². We removed frames with poor qualities ($qi_fact < 1$), or affected by charged particle hits ($saa_sep < 5$), scattered moonlight ($moon_masked = 1$), or artifacts ($cc_flags \neq 0$), and binned the data points every half a year according to the WISE survey strategy. To ensure that the MIR color of the transient can be measured with high precision, we further required that the transient is MIR bright with $m_{\min,W2} < 12.5$, and cause a large amplitude of variation with $\delta W2 > 0.5$ during the NEOWISE-R phase, where $m_{\min,W2}$ and $\delta W2$ are the minimum magnitude in the W2 band and its difference from the maximum value, respectively. Nine TDEs passed our criteria, including AT 2017gge, AT 2018dyk, AT 2018gn, AT 2019dsg, AT 2019qiz, AT 2020nov, AT 2022upj, AT 2023ugy, and SDSS J1115+0544. Note that AT 2018dyk was originally considered to be a changing-look LINER because some of its LC features and spectral characteristics are not common in TDEs (Frederick et al. 2019). However, as its observational data were reanalyzed in more detail and the diversity of TDEs was more fully understood, it was reclassified as TDE (Huang et al. 2023; Clark et al. 2025). In addition, SDSS J1115+0544 was initially reported as a turn-on AGN because the transient remained at a plateau until 600 days after its peak (Yan et al. 2019). However, follow-up works found that it dimmed within 4–5 years, reclassifying it as a slow-evolved TDE (Wang et al. 2022a; Zhang et al. 2025).

Lyu et al. (2022) has investigated the MIR properties of CLAGNs reported in the literature and found 68 CLAGNs with significant MIR variability. We started from Lyu’s sample but removed AT 2018dyk³ and SDSS J1115+0544. We generated the MIR LCs of the remaining 66 objects and selected bright objects with large amplitude variability in the same way as we described previously. One CLAGN, NGC 4151, is too bright, and its photometry was severely affected by saturated pixels, so we removed it from the sample. Finally, a total of 28 CLAGNs passed our criteria. As pointed out by Sheng et al. (2017), the CLAGNs we selected with large amplitudes of MIR variability are likely to originate from changes in the accretion rate, rather than changes in obscuration or other causes.

We collected ANTs from the literature and did the same thing. Eight ANTs passed our criteria, including

AT 2016ezh, AT 2017bgt, AT 2018bcb, AT 2019aal, AT 2019avd, AT 2020agdm, AT 2021loi and AT 2022fpx.

2.2. Quiescent and outburst states

We preliminary analysed the MIR LCs to determine the time duration of quiescent and outburst states.

We selected a quiescent state for each object using an iterative algorithm. For an LC in a particular band, we took the data point with the largest magnitude and those with a magnitude difference of less than 0.2 from it as the initial quiescent state. We then calculated the weighted average of the quiescent state’s magnitudes (weighted by the reciprocal of the squared of the error) and the standard deviation and added data points that differ by less than 0.1 and less than 1.635 standard deviations from the weighted average to the quiescent state. We then recalculated the weighted average and standard deviation with the updated quiescent state and attempted to add new data points to the quiescent state until there were no more data points to add. We calculated the quiescent state for each of the W1 and W2 bands using the above algorithm and finally adopted the intersection of the results of the two bands as the quiescent state of the object. The results are consistent with visual inspections, as shown in Figure 1(a).

We calculated the weighted average of the fluxes in the final quiescent state as the quiescent fluxes. We then calculated excess fluxes f_e by subtracting the quiescent fluxes from the original fluxes and their errors using the law of propagation of uncertainties. For data points not in the quiescent state, we finally selected points where the excess fluxes exceed three times their errors in both W1 and W2 bands as an “outburst state”, as an example shown in Figure 1(b).

The above analysis is based on LCs generated by NEOWISE single-exposure photometries. This method of generating LCs was proved to be reliable (e.g., Jiang et al. 2021); however, it leads to large magnitude errors for faint MIR sources. Thus, for objects with a quiescent W2 magnitude > 11 , we generated LCs using time-resolved coadded data provided by the unWISE project (Meisner et al. 2018) with an image subtraction method, which was also proved reliable (e.g., Masterson et al. 2024). For each object in each band, we made a reference image by combining the quiescent-state images, and then subtracted it from all the images to obtain difference images. We measured flux and error on each difference image using a PSF model whose center is fixed at the optical position for TDEs and ANTs or at the galaxy center for CLAGNs. In addition to routine statistical flux error, we considered the systematic error due to image subtraction, which is 2% of the qui-

² <https://irsa.ipac.caltech.edu/frontpage/>

³ Referred to as SDSS J153308.02+443208.4 in Lyu et al. (2022)

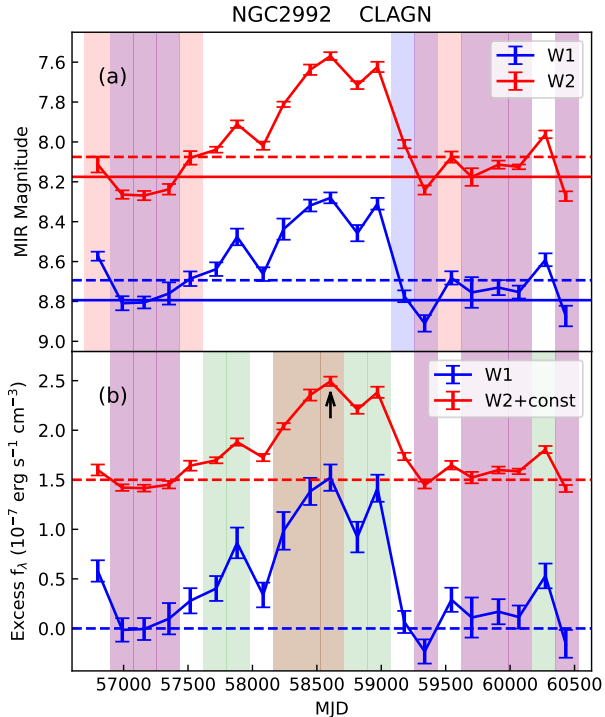


Figure 1. (a): Illumination of selecting quiescent state. The horizontal solid lines show the quiescent levels, and the dashed lines show the magnitude thresholds for selecting the quiescent state. The shades indicate the final quiescent states: shallow blue for the W1 band, shallow red for the W2 band, and shallow purple for their intersection. (b): Illumination of selecting outburst state (green and orange shades) and the rising phase (orange shade). The black arrow labels the peak time.

escent PSF flux according to our tests using galaxies with no outbursts. We adopted the fluxes measured on difference images as excess fluxes f_e , and selected the outburst state in the same way as described previously. In Figure 2, we show an example that the data quality improves by using unWISE data. The flux errors are smaller, and more data points are selected for the outburst state, so the variation of MIR color can be better studied. However, because we have not obtained unWISE data in 2023 and beyond, we still use NEOWISE data for transients that started late, for example, AT 2022fpx, AT 2022upj, and AT 2023ugy.

2.3. Rising phase and further selections

Based on numerical simulations, Sun et al. (2020) demonstrated that the time variation of MIR color in the rising phase is critical to probe the nature of a MIR outburst. Therefore, we selected the rising phase of each outburst for the following analysis.

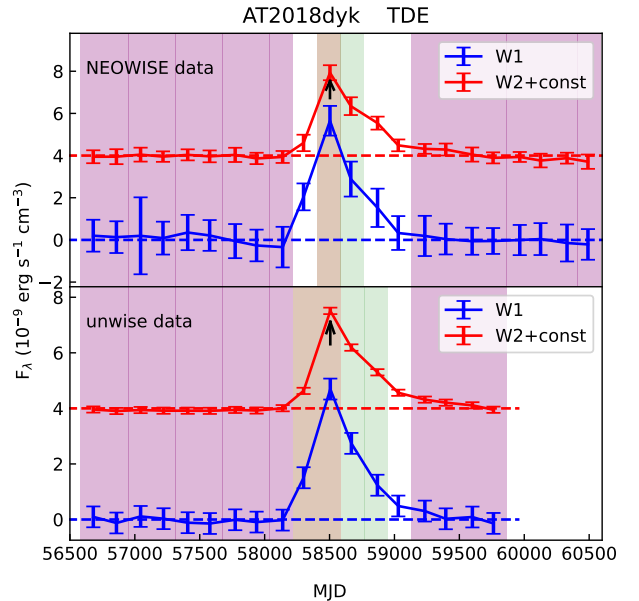


Figure 2. The selections for the outburst state and rising phase for AT 2018dyk. The upper and lower panels are the results using NEOWISE data and unWISE data, respectively. The meaning of labels and colors are the same as Figure 1(b).

We selected consecutive data points in the outburst state with $t \leq t_{\text{peak}}$ as the rising phase, where t_{peak} is the peak time in the W2 band, as examples shown in Figure 1(b) and Figure 2 with orange shades.

We excluded eight CLAGNs because the rising phase may not be completely sampled by NEOWISE-R, which will be described in detail in Appendix A. The final sample contains 37 objects, including 9 TDEs, 20 CLAGNs, and 8 ANTs. We list the redshift, the type and the reference in Table 1.

2.4. MIR properties of the samples

In this subsection, we show the MIR properties of the optically selected transients, including $m_{\text{min},W2}$, $\delta W2$, the peak W2 luminosity $L_{\text{max},W2}$ after quiescent level subtracted, and the rise time t_{rise} . We calculated $L_{\text{max},W2}$ using luminosity distance D_L converted from redshift z if $z > 0.01$, otherwise we used the median value of D_L given by the NASA/IPAC Extragalactic Database⁴. We set the start time of the outburst as between the first data point in the rising phase and the previous data point, and calculated the t_{rise} as the time difference between the start and the peak time in the W2 band. If the rising phase starts at the first data

⁴ <https://ned.ipac.caltech.edu/>

Table 1. Information of the optical transients and parameters of MIR color variation.

Object	RedShift	Type	References	CVR	IC
AT2017gge	0.066	TDE	1,2	–	0.60 ± 0.03
AT2018dyk	0.0367	TDE	3,4,5	1.11 ± 0.62	0.34 ± 0.32
AT2018gn	0.0375	TDE	6	0.33 ± 0.04	0.51 ± 0.05
AT2019dsg	0.0512	TDE	7	0.66 ± 0.15	0.67 ± 0.05
AT2019qiz	0.0151	TDE	7	0.27 ± 0.03	0.60 ± 0.06
AT2020nov	0.084	TDE	8	0.75 ± 0.23	0.31 ± 0.09
AT2022upj	0.054	TDE	9	0.48 ± 0.18	0.52 ± 0.04
AT2023ugy	0.106	TDE	10	0.46 ± 0.42	0.41 ± 0.18
SDSS J1115+0544	0.09	TDE	11,12,13	0.41 ± 0.09	0.68 ± 0.06
AT2016ezh	0.0804	ANT	14,15	0.37 ± 0.06	0.27 ± 0.14
AT2017bgt	0.064	ANT	16	0.41 ± 0.18	0.24 ± 0.28
AT2018bcb	0.1192	ANT	17	–	0.49 ± 0.03
AT2019aalc	0.0356	ANT	18	0.35 ± 0.09	0.43 ± 0.07
AT2019avd	0.0296	ANT	19,20,21,22	0.20 ± 0.04	0.50 ± 0.06
AT2020adgm	0.056	ANT	23	0.56 ± 0.10	0.24 ± 0.09
AT2021loi	0.083	ANT	24	0.35 ± 0.04	0.30 ± 0.03
AT2022fpx	0.073	ANT	25	0.32 ± 0.20	0.42 ± 0.30
2MASX J0938+0743	0.022	CLAGN	26	0.33 ± 0.26	0.40 ± 0.38
2MASS J0948+4030	0.0468	CLAGN	26	0.04 ± 0.21	0.59 ± 0.27
IRAS23226-3843	0.0359	CLAGN	26	0.24 ± 0.16	0.36 ± 0.25
Mrk1018	0.043	CLAGN	26	0.87 ± 0.29	0.36 ± 0.10
NGC0863	0.0264	CLAGN	26	0.08 ± 0.11	0.76 ± 0.16
NGC1566	0.005	CLAGN	26	-0.55 ± 0.29	1.09 ± 0.15
NGC2992	0.0077	CLAGN	26	0.19 ± 0.25	0.66 ± 0.22
NGC3516	0.0088	CLAGN	26	-0.02 ± 0.12	0.64 ± 0.23
NGC4388	0.0084	CLAGN	26	-0.01 ± 0.28	1.28 ± 0.25
SDSS J0813+4608	0.0538	CLAGN	26	0.09 ± 0.12	0.50 ± 0.12
SDSS J0817+1012	0.0458	CLAGN	3,26	-0.02 ± 0.09	0.76 ± 0.22
SDSS J0829+4154	0.1263	CLAGN	26	0.11 ± 0.12	0.19 ± 0.24
SDSS J0915+4814	0.1005	CLAGN	3,26	0.12 ± 0.27	0.55 ± 0.38
SDSS J1133+6701	0.0397	CLAGN	3,26	0.13 ± 0.06	0.47 ± 0.09
SDSS J1225+5108	0.1679	CLAGN	3,26	0.13 ± 0.26	0.50 ± 0.11
SDSS J1625+2415	0.0503	CLAGN	26	0.06 ± 0.21	0.65 ± 0.16
WISEA J0847+1824	0.0848	CLAGN	26	0.16 ± 0.16	0.53 ± 0.33
WISEA J1003+3525	0.1189	CLAGN	26	-0.06 ± 0.06	0.52 ± 0.10
WISEA J1545+1709	0.0483	CLAGN	26	-0.05 ± 0.10	0.71 ± 0.15
WISEA J1545+2511	0.117	CLAGN	26	0.03 ± 0.13	0.55 ± 0.22

References: 1. Wang et al. (2022b); 2. Onori et al. (2022); 3. Frederick et al. (2019); 4. Huang et al. (2023); 5. Clark et al. (2025); 6. Wang et al. (2024); 7. van Velzen et al. (2021); 8. Earl et al. (2024); 9. Newsome et al. (2024); 10. Yao et al. (2023); 11. Yan et al. (2019); 12. Wang et al. (2022a); 13. Zhang et al. (2025); 14. Blanchard et al. (2017); 15. Petrushevska et al. (2023); 16. Trakhtenbrot et al. (2019); 17. Neustadt et al. (2020); 18. Veres et al. (2024); 19. Malyali et al. (2021); 20. Frederick et al. (2021); 21. Chen et al. (2022); 22. Wang et al. (2024); 23. Kosec et al. (2023); 24. Makrygianni et al. (2023); 25. Wiseman et al. (2025); 26. Lyu et al. (2022).

point of NEOWISE-R, or the outburst peaks at the last data point of the LC, we set the t_{rise} calculated above as the lower limit. In addition, as can be seen from Figure A2, TDE AT 2017gge and ANT AT 2018bcb peaks

at the first data point of the outburst state, and hence, we could only calculate the upper limit of t_{rise} for them.

We show the distribution of $m_{\text{min,W2}}$ and $\delta W2$ in Figure 3(a). CLAGNs generally cause smaller amplitude of variability with $\delta W2 < 1.7$ magnitude, while TDEs and

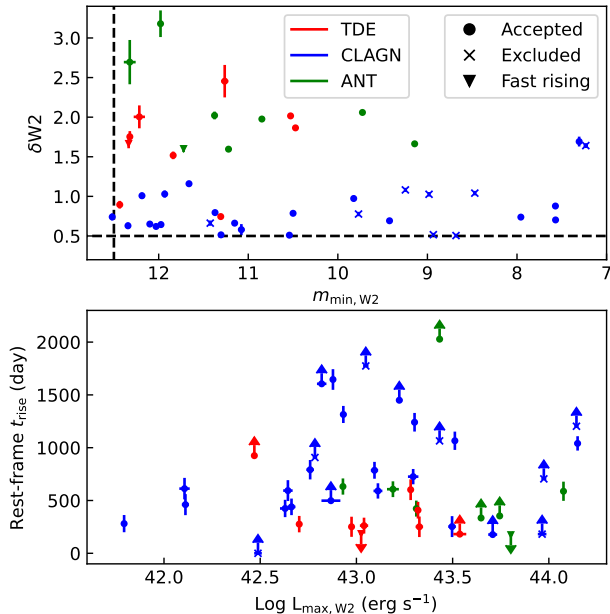


Figure 3. MIR properties of the final sample (dots) and the excluded CLAGNs (crosses). The upper panel shows $m_{\min, W2}$ and $\delta W2$, and the lower panel shows $L_{\max, W2}$ and t_{rise} . TDEs, ANTs and CLAGNs are shown in red, green and blue symbols. The two fast-rising objects (AT 2017gge and AT 2018bcb) are marked with inverted triangles. Note that one excluded CLAGN, NGC 4395, has a luminosity of $L_{\max, W2} = 10^{39.4} \text{ erg s}^{-1}$ and is outside the scope of the lower panel.

ANTs can cause variation with $\delta W2$ up to ~ 3 magnitude. We also show the distribution of $L_{\max, W2}$ and t_{rise} in Figure 3(b). The MIR luminosities $L_{\max, W2}$ of the sample are mainly in the range of $\sim 10^{42} - 10^{44} \text{ erg s}^{-1}$. The TDEs generally have lower MIR luminosities than ANTs as the median values of $L_{\max, W2}$ are $\sim 10^{43}$ and $\sim 10^{43.6} \text{ erg s}^{-1}$, respectively. The rise time of the sample is distributed over a wide range between < 200 days and > 2000 days. TDEs and ANTs generally have shorter rise time than CLAGNs, as among the 16 objects whose t_{rise} is > 2 years, only one is TDE, and one is ANT, and the rest are CLAGNs.

The eight CLAGNs excluded in section 2.3 have similar properties to other CLAGNs, so excluding them would not change the overall properties of the sample. This was reasonable because they were excluded due to the inappropriate start time for a detailed study of the rising phase.

3. ANALYSIS OF MIR COLOR VARIATION AND RESULTS

This section studied the MIR color variation of the optically selected outbursts in the rising phase. We did not calculate the dust temperature as some previous works

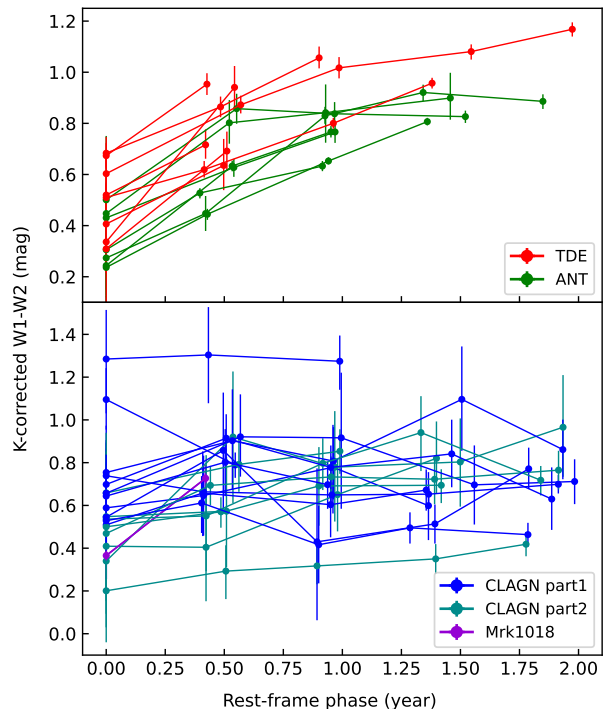


Figure 4. Time variation of MIR color in the rising phase. The upper panel shows TDEs (red) and ANTs (green), and the lower panel shows CLAGNs. For clarity, we split the CLAGN sample into two parts, one with $\text{CVR} < 0.1$ (blue) and the other with $\text{CVR} > 0.1$ (dark cyan). We labelled CLAGN Mrk 1018 with special color variation using purple.

had done (e.g., Jiang et al. 2017; Reynolds et al. 2022). This is because the dust temperature depends heavily on the spectral energy distribution (SED), and its relationship with the directly observed quantity is complicated, making its error difficult to analyze. Instead, we used K-corrected MIR color $W1 - W2$, i.e. color in the rest frame, as a probe of dust temperature. We describe how we applied the K-correction and estimated the systematic error introduced by the K-correction in Appendix B.

We calculated the color of the excess flux after subtracting the quiescent state flux. We did not use the total flux because it contains emission from the host galaxy, which is unrelated to the outburst. For outbursts occurring in AGNs, like CLAGNs and ANTs, the echoing dust is likely the AGN dusty torus, and hence the color we measured may present the change in dust temperature, rather than the temperature itself. We will analyze this effect in section 4.1.2.

3.1. Time variation of MIR color in the rising phase

We calculated the K-corrected MIR color in the rising phase for all 37 objects. In Figure 4, we show the varia-

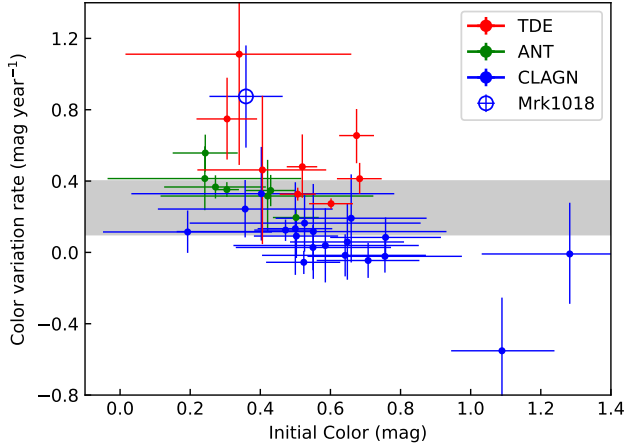


Figure 5. The distribution of ICs and CVRs of the optically selected sample. Red, green and blue represent TDE, ANT, and CLAGN, respectively. We specifically marked Mrk 1018, whose type is uncertain. We show the CVR thresholds used to distinguish TDE, ANT and CLAGN in a grey shade.

tion of MIR color over time, grouped by different types. For objects with $t_{\text{rise}} > 2$ years, we only show variation in the first two years.

The MIR color of TDEs and ANTs generally turns red (increases) quickly during the rising phase, while that of CLAGNs shows no significant trend, either unchanged or turning red slowly. In addition, the color of ANTs is generally bluer than TDEs at the same phase.

To quantify these differences, we fit the time variation of color using a linear function and adopted the slope as color variation rate (CVR), and calculated its error using the Monte Carlo method. We also adopted the color of the first point in the rising phase as the initial color (IC). Note that AT 2017gge and AT 2018bcb have only one data point in the rising phase, so CVR could not be calculated. We list the CVRs for the remaining 35 objects and the ICs for all 37 objects in Table 1.

As seen from Figure 5, TDEs and ANTs have overall larger CVRs than CLAGNs. The CVRs of 8 TDEs are between 0.27 and 1.11 mag yr⁻¹ with a median of 0.47, and those of 7 ANTs are between 0.20 and 0.56 mag yr⁻¹ with a median of 0.35, and those of 20 CLAGNs are between -0.55 and 0.88 mag yr⁻¹ with a median of 0.09. We checked the statistical significance of the difference in CVR distributions across TDEs, ANTs and CLAGNs using the Kolmogorov-Smirnov (K-S) test. The difference between TDEs and CLAGNs (ANTs and CLAGNs) is significant as the probability corresponding to the K-S statistic is 2.9×10^{-5} (3.1×10^{-4}). At the same time, there is no significant difference between TDEs and ANTs. In addition, the median IC of 8 ANTs (in-

cluding AT 2018bcb) is 0.36 mag, smaller than 0.52 mag, the median of 9 TDEs (including AT 2017gge), and the difference between IC distributions is also significant according to the K-S test as the probability is 0.020.

The above analyses do not take into account the influence of measurement errors. In general, for large enough sample sizes, measurement errors would cause the distribution of observed values to be more diffuse than that of the true values, which weakens the statistical significance of the difference between two distributions. Therefore, the difference in CVR/IC distributions cannot be explained by measurement errors.

Among the 20 CLAGNs, Mrk 1018 has a CVR of 0.87 ± 0.29 mag yr⁻¹, significantly higher than other CLAGNs and similar to TDEs and ANTs. Despite that Mrk 1018 is a famous CLAGN with long-term, large-amplitude variability along with state transition (e.g., Cohen et al. 1986; Husemann et al. 2016), it met our criteria because of its giant outburst in 2020 (Brogan et al. 2023; Lu et al. 2025). We analyzed the optical LCs of Mrk 1018 during this outburst and present the results in Appendix C. In brief, the lack of data makes it difficult to distinguish whether it is closer to typical CLAGN outbursts or ANTs like AT 2017bgt. Therefore, we removed Mrk 1018 in the following analysis of the MIR colors of the sample because its type is uncertain.

3.2. Distinguishing TDEs/ANTs from CLAGNs

Since TDEs/ANTs generally have larger CVRs than CLAGNs, we considered distinguishing TDE/ANT from CLAGN using the maximum CVR of CLAGNs and the minimum CVR of TDE+ANTs. In the current sample, the maximum of the 19 CLAGNs (excluding Mrk 1018) is 0.33 mag yr⁻¹, while the minimum of the 15 TDE+ANTs is 0.20 mag yr⁻¹. However, these values have two uncertainties, one from sampling and the other from measurement error.

We first considered the impact of these uncertainties on the maximum of CLAGNs. The sampling leads to underestimation of the maximum, while measurement error leads to overestimation when the sample size is large enough. The two uncertainties lead to opposite effects, whose strengths are related to the sample size, the intrinsic scatter of CLAGNs' CVRs, and the level of errors. To quantitatively assess which effect is more substantial, we ran a simulation. In the simulation, we assumed that the current observed values were true and evaluated the effects of sampling and measurement error using bootstrap and Monte Carlo methods, respectively. Simulations show that the fake sample overestimated the maximum 97.5% of the time, indicating that the over-

estimation caused by measurement error dominates the underestimation caused by sampling. According to the simulation, the probability of the fake sample overestimating the maximum or underestimating by $< 0.07 \text{ mag yr}^{-1}$ is as high as 99.3%. Therefore, we considered it safe to set the upper limit of CLAGNs' CVR at 0.4 mag yr^{-1} .

We then analyzed the minimum CVR of TDE+ANTs similarly. We found that the underestimation of the minimum caused by measurement error dominates the overestimation caused by sampling. Similarly, we adopted a safe lower limit of TDE+ANTs' CVR at 0.1 mag yr^{-1} , which underestimates the true value by $> 99.9\%$ according to the simulations.

We finally divided Figure 5 into three regions based on the two thresholds of CVRs (grey shades): region U with $\text{CVR} > 0.4 \text{ mag yr}^{-1}$ representing a high probability of TDE or ANT, region L with $\text{CVR} < 0.1 \text{ mag yr}^{-1}$ representing a high probability of CLAGN, and region M with $0.1 \leq \text{CVR} \leq 0.4 \text{ mag yr}^{-1}$, where the type of the object is difficult to determine.

The CVR could not be calculated for AT 2017gge and AT 2018bcb because they rise too fast relative to the cadence of WISE. Both objects are TDE or ANT, consistent with that TDEs/ANTs generally have shorter t_{rise} than CLAGNs (section 2.4). This means an object rising too fast to calculate CVR is more likely to be TDE/ANT than CLAGN. However, the confidence level of this judgement is not high due to the small sample sizes.

4. EXPLANATIONS FOR DIFFERENCES IN MIR COLOR VARIATIONS

In this section, we explore the possible explanations of the differences in MIR color variation between different types of outbursts with the help of simulations. The main phenomena we need to explain are: 1. TDEs' and ANT's MIR colors turn red faster than CLAGNs' in the rising phase, as the median CVR of TDE+ANTs is $\sim 0.3 \text{ mag yr}^{-1}$ larger than that of CLAGNs; 2. ANT's are bluer than TDEs when they begin, as their median IC is smaller than TDEs.

We simulated the IR LCs of dust echoes of TDEs, ANT's and CLAGNs using a dust radiative transfer model developed by Lu et al. (2016) and Sun et al. (2020). We considered a transient UV source in the galaxy center heats dust grains to generate IR reradiation in a spherical shell. The LC of the transient source is described as $L_{\text{UV}}(t)$. The dust shell has an initial inner radius of r_{in} and an outer radius of r_{out} , the dust composition is a standard ISM mixture of 47% graphite and 53% silicate, and the dust grain has a radius of

a_0 and a number density of n_d . The model calculates IR LCs by considering the dust's inner radius change caused by sublimation, the time delay of IR reradiation due to the light travel time effect, and the absorption of emergent IR emission by the dust structure itself.

We investigated the influence of each parameter on the MIR color variation using the control variable method. We display the influence of different UV LCs in section 4.1, and the influence of different echoing dusts in section 4.2, and finally discuss possible explanations of different CVR and IC in section 4.3.

4.1. The difference in UV LCs

4.1.1. Influence of shape of UV LC

The shapes of UV LCs of TDEs and ANT's generally differ from those of CLAGNs. TDEs typically rise of $\sim 10 - 50$ days, peak of 1-3 months, and fade of months to years (e.g., van Velzen et al. 2020; Yao et al. 2023), and ANT's have similar UV LCs to TDEs. However, the LCs of CLAGNs are not regular, and their rises are slower with rise time usually between months to years (e.g., Ricci & Trakhtenbrot 2023).

To reflect this difference in the shape of UV LC, we tried four forms of UV LC. The first is a TDE form where L_{UV} rises rapidly and fade slowly as $L \propto t^{-5/3}$:

$$L_{\text{UV}}(t) = \begin{cases} 0 & , t < t_0 \\ L_{\text{max}} \left(1 + \frac{t-t_0}{\tau_1}\right)^{-5/3} & , t > t_0, \end{cases} \quad (1)$$

where t_0 is the outburst time, L_{max} is the peak UV luminosity and τ_1 describes the rate of fading. The second is an EXP form where L_{UV} rises rapidly and fade exponentially:

$$L_{\text{UV}}(t) = \begin{cases} 0 & , t < t_0 \\ L_{\text{max}} e^{-\frac{t-t_0}{\tau_2}} & , t > t_0, \end{cases} \quad (2)$$

The third is a LINEAR form where L_{UV} rises and falls linearly with similar rising and falling time scales, and the LC is described as:

$$L_{\text{UV}}(t) = \begin{cases} L_{\text{max}} \frac{t-t_0}{\tau_3} & , t_0 < t < t_0 + \tau_3 \\ L_{\text{max}} \left(2 - \frac{t-t_0}{\tau_3}\right) & , t_0 + \tau_3 < t < t_0 + 2\tau_3 \\ 0 & , \text{else,} \end{cases} \quad (3)$$

And the fourth is a FLAT form expressed as:

$$L_{\text{UV}}(t) = \begin{cases} L_{\text{max}} & , t_0 < t < t_0 + \tau_4 \\ 0 & , \text{else,} \end{cases} \quad (4)$$

We referred to the duration τ of an outburst as the ratio of the total energy to the peak luminosity:

$$\tau = \frac{\int_{-\infty}^{+\infty} L(t)dt}{L_{\max}} \quad (5)$$

For the four forms, τ equals to $\frac{2}{3}\tau_1$, τ_2 , τ_3 and τ_4 , respectively.

We studied the influence of the shape of UV LC on the MIR color variation when the L_{\max} is fixed at 10^{44} erg s $^{-1}$ and τ is fixed at 10^7 s. In simulations hereafter, we set the default value of initial inner radius r_{in} as $0.6r_{\text{sub}}(L_{\max})$, where r_{sub} is the sublimation radius corresponding to L_{\max} , and is calculated as (e.g., Peterson 1997):

$$r_{\text{sub}}(L_{\max}) = 0.4 \left(\frac{L_{\max}}{10^{45} \text{ erg s}^{-1}} \right)^{1/2} \text{ pc}, \quad (6)$$

The model can calculate a new inner radius by taking the dust sublimation into account, and hence the value of r_{in} has little influence on the IR LCs when it is less than $0.8r_{\text{sub}}$. In addition, the default values of r_{out} , a_0 and n_d are 1 pc, $0.1 \mu\text{m}$ and 10^{-8} cm^{-3} , respectively.

As shown in Figure 6, the MIR color curves in the rising phases are different. For the TDE and EXP forms, initially, the MIR color is relatively blue and becomes red continuously in the rising and fading phases. While for the LINEAR and FLAT forms, the MIR color turns slightly blue or keeps steady with the rapid rise of luminosity in the early time, and then keeps a blue color near the peak, and finally turns red as it fades. We sampled the simulated MIR color curve at 180-day intervals and calculated IC and CVR in the rising phase using the sampled data. IC and CVR are not definite values but in a range because of the uncertain sampling time, expressed as the time delay t_{delay} between the first sampling and the outburst time. We found that the form of LC has little effect on the IC, but affected the CVR: CVR is 0.2–0.4, 0.15–0.35, -0.1 – -0.2 and ~ 0.05 mag yr $^{-1}$ for TDE, EXP, LINEAR and FLAT forms. We also tried other forms of UV LC with more complicated models. By summarizing these results, we found that to produce a large CVR of $\gtrsim 0.3$ mag yr $^{-1}$, the UV LC needs to contain a rapid rise, a short peak, and a long tail. The reason is that the echoes of the peak luminosity and the long tail have blue and red MIR colors, respectively, and in the rising phase, the fraction of the echo of the long tail is increasing, causing the MIR color to turn red continuously.

4.1.2. Influence of underlying AGN

ANTs and CLAGNs occur in AGNs with long-lived IR emission from the dusty torus. The underlying

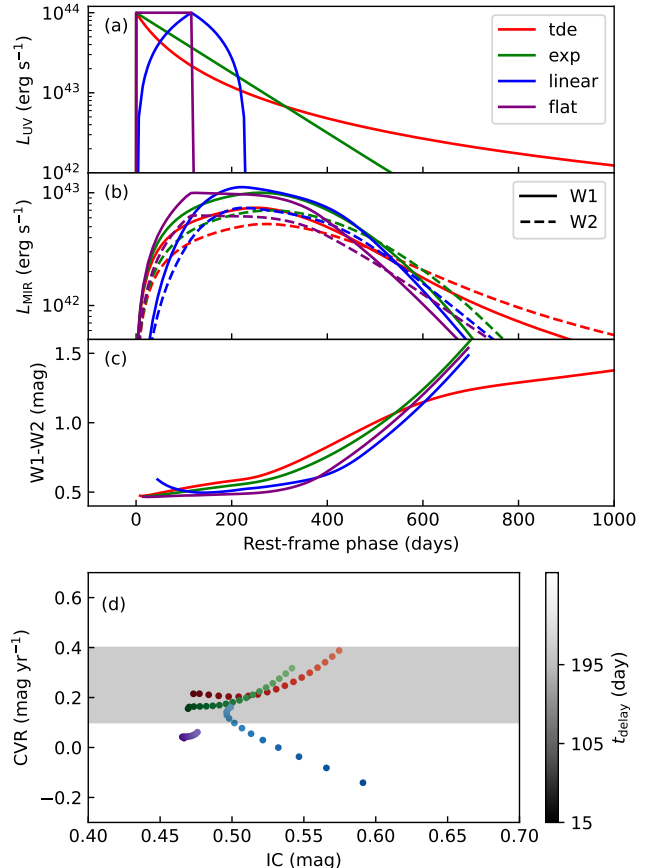


Figure 6. (a): The assumed UV LCs with TDE (red), EXP (green), LINEAR (blue) and FLAT (purple) forms. (b): The simulated MIR LCs in the W1 (solid) and W2 (dashed) bands. (c): The inferred W1-W2 color curves. (d): The IC and CVR calculated using the MIR color data points sampled every 180 days. Values assuming different sampling times are differentiated by color saturations.

AGN causes multiple simultaneous effects, and we explored these effects using simulations. We added a long-standing AGN component with a luminosity L_{AGN} of 10^{43} – 10^{44} erg s $^{-1}$ to the UV LC. We tried UV LC in TDE and LINEAR forms, with L_{\max} of 10^{44} erg s $^{-1}$ and τ of 10^7 s. Note that we subtracted the quiescent fluxes when calculating the MIR color in Section 3, so in the simulation, we also calculated the MIR color after subtraction the IR luminosities of the underlying AGN (the values at $t \leq t_0$). The results are shown in Figure 7.

We found that for the TDE form UV LC, as the ratio of AGN luminosity to the peak outburst luminosity is larger, indicating a smaller amplitude of variability, both the CVR and IC are smaller and deviate more from the values without AGN. While for the LINEAR form UV LC, underlying AGNs little affect the median value of

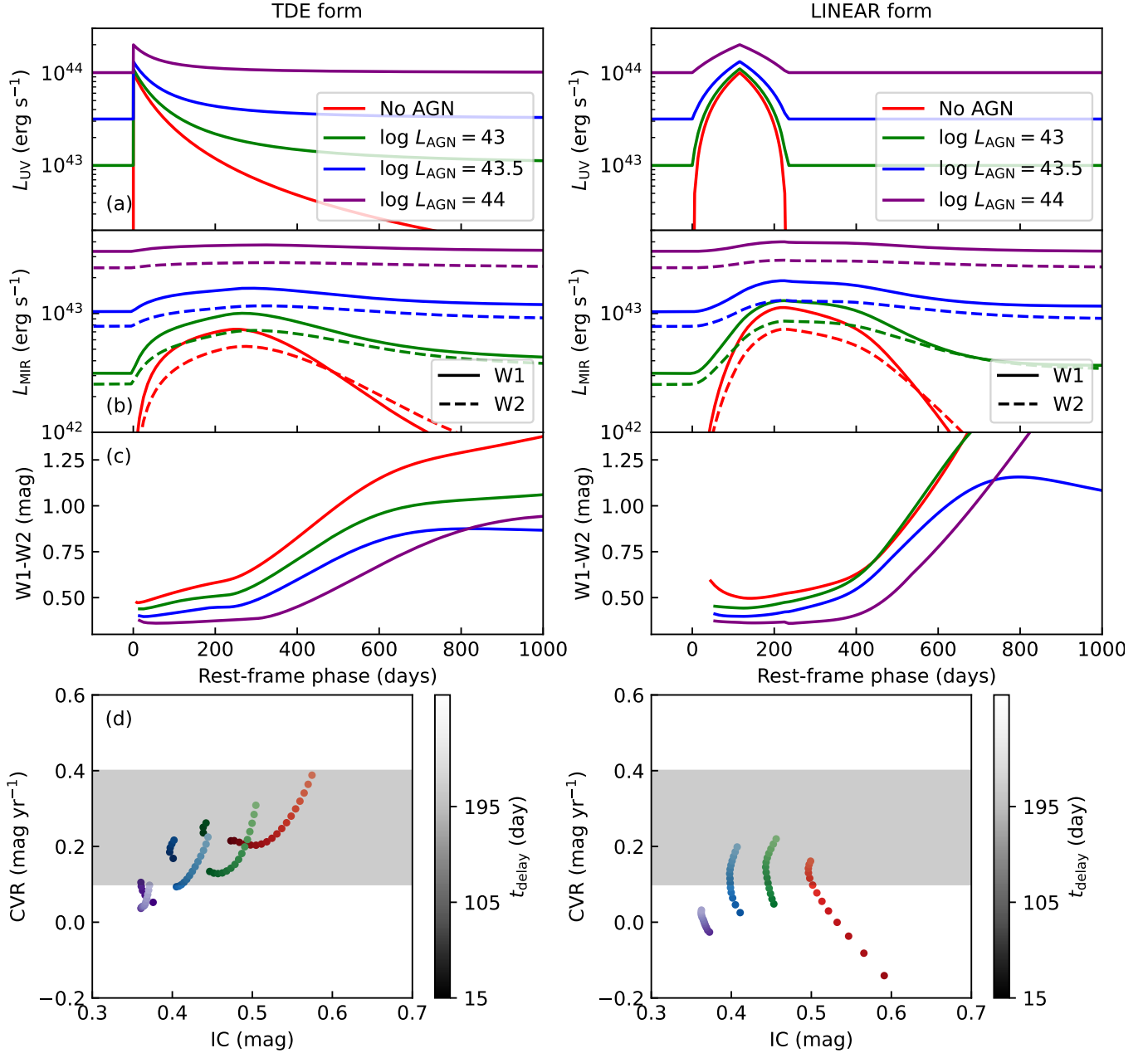


Figure 7. Simulations exploring the influence by underlying AGN. The meanings of panels (a) to (d) are the same as Figure 6. Left panels show simulations assuming TDE-form UV LCs, and right panels show those assuming LINEAR-form UV LCs.

CVR. Thus, in order to produce a large CVR, there must be no AGN or a relatively small AGN contribution.

ANTs generally have large amplitudes of variability: optical ANTs can be brightened by $\gtrsim 2 - 3$ magnitudes in the UV bands at peak. Thus, the AGN contribution results in ANTs having smaller CVRs than TDEs, but the difference between the two is no more than ~ 0.1 mag yr $^{-1}$. On the other hand, most CLAGNs have smaller amplitudes of UV variability of $\lesssim 1 - 2$ magnitudes. Thus, even if a CLAGN happened to have a UV LC

similar to those of TDEs, its CVR would not be large, in the case that it does not vary sufficiently.

In addition, we also explored the influence of the peak UV luminosity and duration on IC and CVR. We show the results in detail in Appendix E.1, and in brief, these two factors could not explain the differences in CVRs and ICs between different types of outbursts.

4.2. Difference in echoing dust

4.2.1. Influence by dust properties

The chemical composition and grain radius of the dust influence the MIR color. As shown in Figure B1(a), graphite dust is bluer than silicate dust at the same temperature. Moreover, the sublimation temperature of graphite (~ 1900 K) is higher than that of silicate (~ 1500 K), resulting in a much higher MIR color of graphite (~ 0.2 mag) than silicate (~ -0.3 mag) at around sublimation temperature. Thus, the difference in dust composition can affect the IC: a higher fraction of graphite results in a bluer MIR color (smaller IC). Dust grains with different radii with the same composition show a small difference in color of 0.1–0.2 mag at the same temperature. Thus, the grain radius may slightly affect the IC. Although we have some knowledge of the dust properties in AGNs, those in TDEs are poorly constrained by observations. Future JWST MIR spectroscopic observations may constrain the dust properties in TDEs, check whether they differ from AGNs, and explore if they can explain the observed IC difference between TDEs and ANTs.

Does the difference in dust properties affect CVR? Answering this question requires considering that dust composition may be dependent on locations. Assuming that the initial dust is a mixture of graphite and silicate, the innermost region of the final dust structure would have a high graphite fraction because the sublimation radius of the graphite is larger than that of the silicate. After taking this effect into account, the color difference between the inner region (arrives earlier) and the outer region (arrives later) would be larger, resulting in a larger CVR. However, this effect may work in both TDE and CLAGN, so it might not explain the difference in CVR between the two samples.

4.2.2. Influence by dust shape

The emergent optical depth of the dust structure significantly affects IC according to our simulations (Appendix E.2). The IC increases (redder) with the increase of the emergent optical depth. The difference in the radial optical depth of the dust structure or the difference in the dust geometry may cause a difference in the emergent optical depth. An example of the latter is that the IR echo of a face-on torus, which mainly comes from the inner region, has a smaller emergent optical depth than a spherical shell or edge-on torus with the same radial optical depth.

The pc-scale dust structures in active galaxies generally have torus shape, as indicated by the AGN unified model (e.g. Antonucci 1993). However, there is no clear evidence for the anisotropy of nuclear dust structure in inactive galaxies. The ANT samples are selected in the optical band, and hence, their toruses are more likely to

be face-on. Thus, the difference in the dust geometry can explain why ANTs have smaller ICs than TDEs.

4.3. Promising explanations

According to simulations in section 4.1, in order to produce a large CVR, the UV LC must meet two conditions, one is that the LC of the outburst must be characterized by “rapid rise, short peak and long tail”, and the other is that there is no or relatively weak underlying AGN. The CVR difference between TDEs/ANTs and CLAGNs could be related to these two factors, while could hardly be associated with the differences in peak luminosities or durations. In addition, we did not prefer explanations involving differences in dust structure or in dust properties, because ANTs and CLAGNs both occur in AGNs and there is no clear reason why their dust environments are different.

We preferred to explain the smaller ICs in ANTs than in TDEs by differences in dust structure or dust property, because the two types of outbursts have similar UV LCs. Possible explanations include differences in dust chemical composition, in radial optical depth of the dust structure, and in dust geometry. Among them, the difference in dust geometry (face-on torus in ANTs versus spherical shell in TDEs) is supported by observations and hence is promising. If this factor is indeed dominant, we predicted that the IC difference between TDEs and ANTs in MIR samples would be smaller or even disappear, because dusty toruses in MIR selected ANTs should have larger inclinations than optically selected ANTs.

5. APPLYING TO MIR OUTBURSTS

As we have developed a new method to distinguish TDEs/ANTs from CLAGNs, we applied it to samples of MIR outbursts. The samples included the MIRONG sample of Jiang et al. (2021) and the WTP sample of Masterson et al. (2024).

5.1. MIRONG sample

The MIRONG sample contains 137 MIR outbursts. We removed four supernovae and four objects with strong radio emissions that may be associated with a jet, all identified by Jiang et al. (2021). We also removed two objects that contain problematic data points. We reduced the data for the remaining 127 objects and selected quiescent and outburst states and the rising phase as we did for the optically selected sample. The only difference is that we did not require $m_{\min, W2} < 12.5$ or $\delta W2 > 0.5$ here. In this process, we removed 12 objects whose rising phase began at the first data point of NEOWISE-R. We also removed nine objects with only

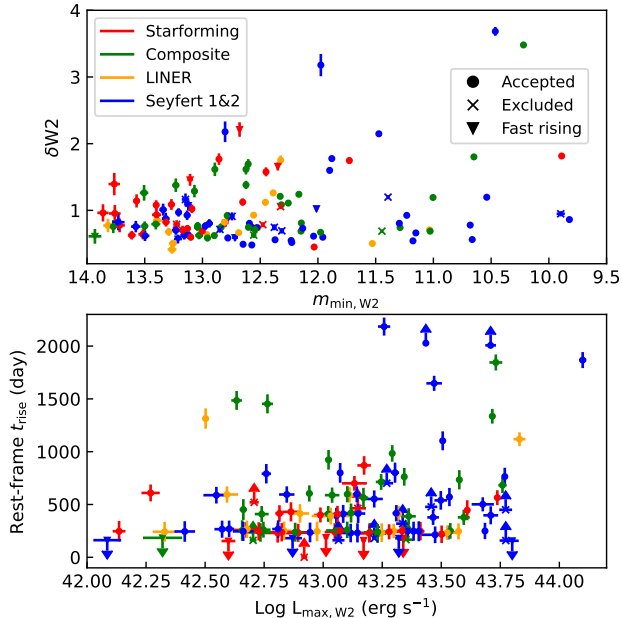


Figure 8. MIR properties of the MIRONG sample. The upper panel shows $m_{\min,W2}$ and $\delta W2$, and the lower panel shows $L_{\max,W2}$ and t_{rise} . Star-forming, Composite, LINER and Seyfert galaxies are shown in red, green, orange and blue symbols. Note that the objects in Jiang et al. (2021) with broad emission lines (Seyfert 1) and those with Seyfert-like narrow line ratios (Seyfert 2) were both treated as Seyfert galaxies in this work. The meanings of symbols (dot, cross and inverted triangle) are the same as Figure 3.

one data point in the rising phase. Finally, there are 106 objects left for the following analysis.

The MIR properties of the 106 objects and the 21 objects removed when selecting the rising phase are displayed in Figure 8. The MIR luminosity $L_{\max,W2}$ of the sample is in the range of $\sim 10^{42} - 10^{44}$ erg s $^{-1}$, and the rise time t_{rise} is in the range of < 200 and > 2000 days. These ranges are similar to those of the optically selected sample, and hence, this sample is suitable for the method distinguishing TDE/ANT and CLAGN developed in section 3.

We calculated the IC and CVR of the 106 MIR outbursts in the same way as we did for the optically selected sample. Using a Monte Carlo method, we calculated the errors of IC and CVR, and also the probability that each object falls in the U, M, and L regions (p_U , p_M and p_L) defined in section 3.2. We list these results in Appendix D.

We show the distribution of ICs and CVRs in Figure 9, grouped into four subsamples according to the host galaxy type. We made K-S tests to check whether the IC and CVR distributions are different among the subsamples. The tests showed that there was no differ-

Table 2. Numbers of MIR outbursts falling into the three regions.

	N_U	N_M	N_L	E_U	E_M	E_L
non-Seyfert (68)	23	27	18	21.9	22.4	23.7
Seyfert (38)	6	17	15	8.2	14.1	15.7
WTP (15)	3	10	2	3.9	6.0	5.2

ence among star-forming ($N = 22$), composite ($N = 31$) and LINER ($N = 15$) galaxies. At the same time, there was a slight difference between CVRs of Seyfert ($N = 38$) and non-Seyfert galaxies (the union of the other three, $N = 68$) with a significance of 0.094 (Figure 9(d)). The difference can also be seen from the median values: the median CVR of non-Seyfert galaxies is 0.27 mag yr $^{-1}$, which is between those of optically selected TDEs (0.47) and CLAGNs (0.09), while the median CVR of Seyfert galaxies is 0.13 mag yr $^{-1}$, close to that of CLAGNs.

According to the best measurements of CVRs, we counted the numbers of MIR outbursts falling into the three regions (N_U , N_M and N_L) for non-Seyfert and Seyfert galaxies. We also calculated the expected value of the numbers in each region (E_U , E_M and E_L) based on the probability that each source falls in the region: $E_U = \sum_i p_{U,i}$, $E_M = \sum_i p_{M,i}$, and $E_L = \sum_i p_{L,i}$, where $p_{U,i}$, $p_{M,i}$ and $p_{L,i}$ are the probability that the i th object falls into the corresponding region. The results are listed in Table 2. Both calculations yield estimations of the numbers of truth CVR values falling into each region. Considering the objects in the M region and the objects that were excluded when selecting the rising phase, in the non-Seyfert subsample, $\gtrsim 22 - 23$ are TDEs and $\gtrsim 18 - 24$ are CLAGNs, and in the Seyfert subsample, $\gtrsim 6 - 8$ are ANTs and $\gtrsim 15 - 16$ are CLAGNs. Therefore, we concluded that the MIRONG sample is a mixture of TDEs/ANTs and CLAGNs, and this is the case for MIR outbursts in both non-Seyfert and Seyfert galaxies.

5.2. WTP sample

The WTP sample contains 18 MIR outbursts, including 12 in their gold subsample and 6 in their silver subsample. We analyzed their MIR LCs like we did for the MIRONG sample. We excluded WTP15acbuuv, whose rising phase began at the first data point of NEOWISE-R, and WTP14adbjsh and WTP16aaqrer, which have only one data point in the rising phase. Finally, there are 15 objects left for the following analysis.

The MIR properties of the 15 objects and the three excluded objects are displayed in Figure 10. The MIR

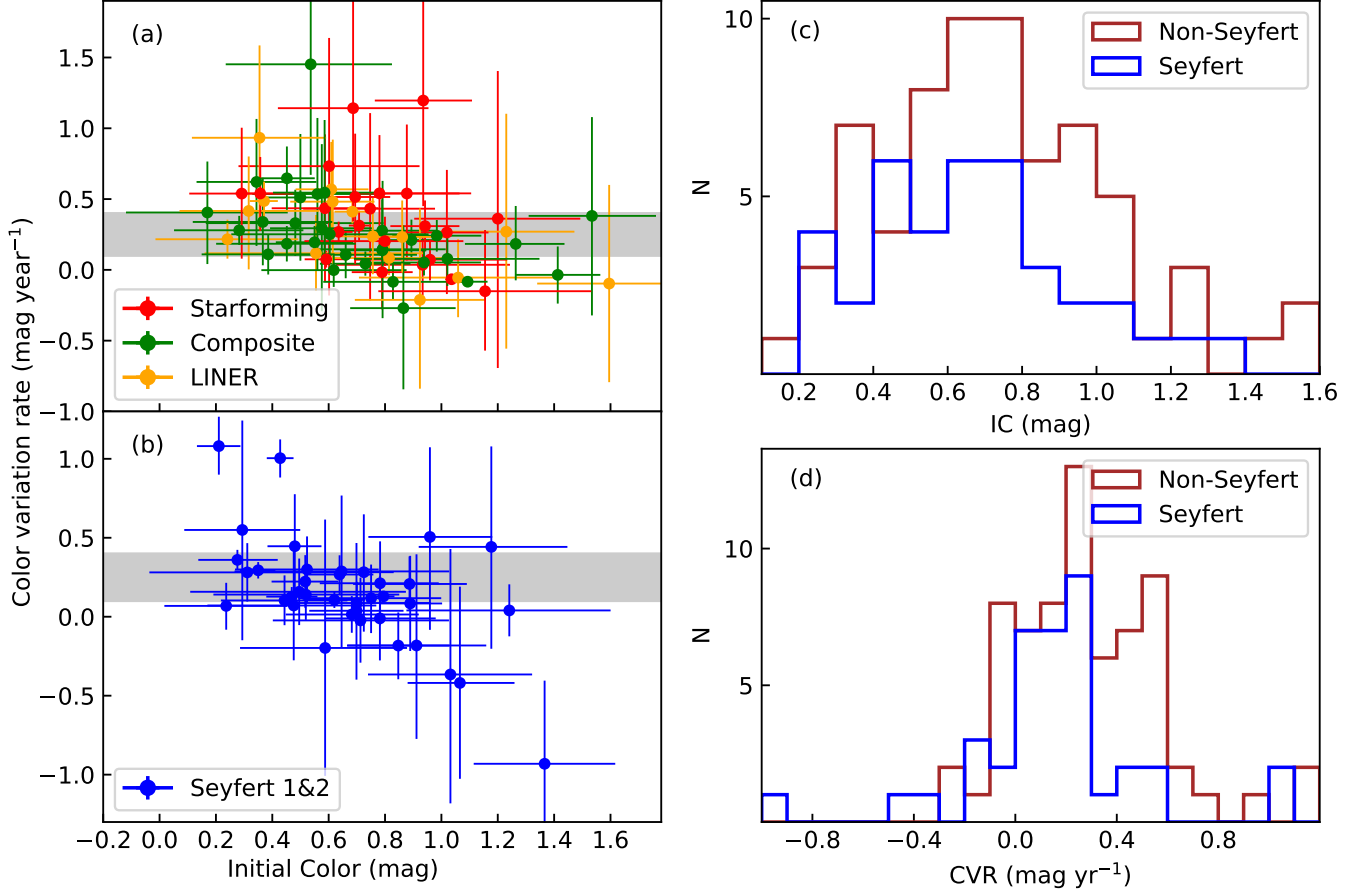


Figure 9. Distribution of ICs and CVRs of the MIRONG sample. Panel (a) shows star-forming (red), composite (green) and LINER (orange) galaxies and panel (b) shows Seyfert galaxies (blue). We compare the distributions of ICs for non-Seyfert and Seyfert galaxies in panel (c) and those of CVRs in panel (d).

luminosity $L_{\max, W2}$ of the sample is in the range of $\sim 10^{42} - 10^{43.5}$ erg s⁻¹, lower than the optically selected sample. This may be because M24 limited the distance to < 200 Mpc for the sample. The rise time t_{rise} is in the range of < 200 and ~ 1000 days, shorter than the optically selected sample. This is because M24 required a rapid rise in the MIR LC.

For the 15 MIR outbursts, we calculated IC, CVR, and the probabilities in the three regions and list the results in Appendix D. We show the distribution of ICs and CVRs in Figure 11. We found no statistical differences in the parameters of gold and silver subsamples divided by M24, probably because there is no intrinsic difference or the sample sizes are too small, so we did not distinguish the two subsamples in the following analysis. The median CVR of the WTP sample is 0.19 mag yr⁻¹, between those of optically selected TDEs (0.44) and CLAGNs (0.09).

We also counted the number of outbursts in the three regions and calculated the expected value of numbers in the same way as we did for the MIRONG sample, and

list the results in Table 2. In the WTP sample, $\gtrsim 3 - 4$ are TDEs, and $\gtrsim 2 - 5$ are CLAGNs. Therefore, we concluded that the WTP sample is also a mixture of TDEs and CLAGNs.

5.3. Promising TDE candidates

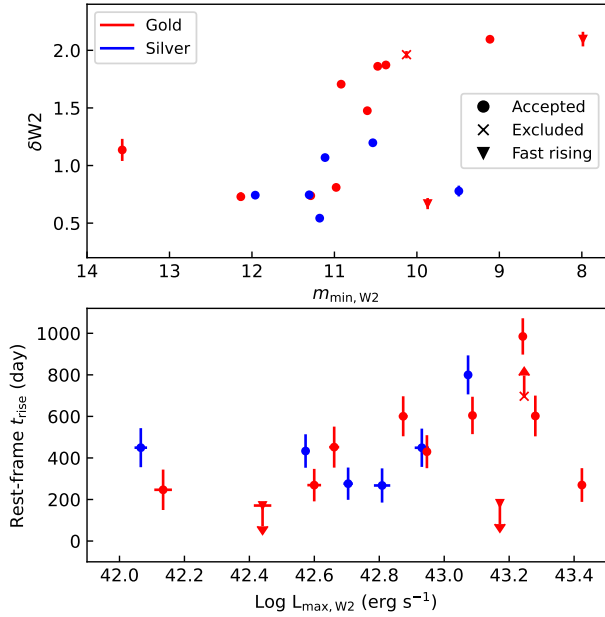
In this subsection, we selected promising TDE candidates for use in subsequent studies.

We selected MIR outbursts in MIRONG and WTP samples that have a probability of falling into U region p_U of $> 70\%$, and are hosted in non-Seyfert galaxies. There are eight outbursts, seven from the MIRONG sample and one from the WTP sample. We list the MIR information of these TDE candidates in Table 3.

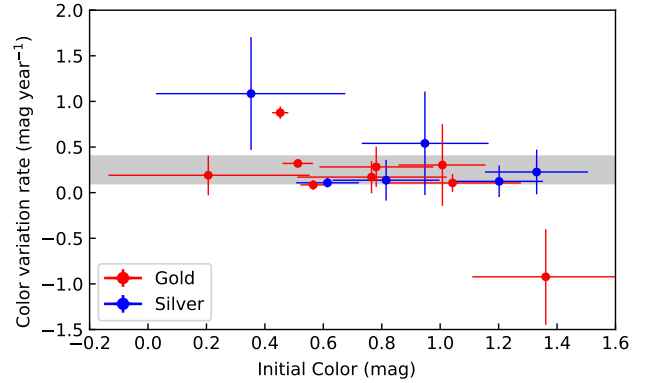
There should be more TDEs in the MIR samples than these candidates. For example, if the p_U criterion is applied to the six optical TDEs whose CVRs can be measured, only two (AT 2019dsg and AT 2020nov) can pass. In addition, the MIR samples are fainter on average, leading to larger measurement errors of CVRs, and hence, it is more difficult to pass the p_U threshold.

Table 3. Promising TDE candidates.

Object	RedShift	Sample	CVR	IC	p_U	$m_{\min, W2}$	$\delta W2$	$\log L_{\max, W2}$	t_{rise}
WTP17aamoxe	0.042	WTP(Gold)	0.88 ± 0.07	0.45 ± 0.03	100.00%	10.38	1.87	43.42	270 ± 81
SDSS J0837+4143	0.09806	MIRONG(Comp)	1.45 ± 0.80	0.54 ± 0.29	90.63%	12.15	0.69	43.20	236 ± 90
SDSS J1513+3111	0.07181	MIRONG(Comp)	0.65 ± 0.22	0.45 ± 0.10	86.13%	12.17	1.24	43.10	260 ± 78
SDSS J1053+5524	0.15174	MIRONG(SF)	1.20 ± 0.74	0.94 ± 0.17	85.49%	13.10	0.60	43.20	227 ± 86
SDSS J1628+4810	0.12454	MIRONG(SF)	1.14 ± 0.80	0.69 ± 0.27	82.26%	13.61	0.63	42.82	237 ± 87
SDSS J1409+1057	0.05972	MIRONG(LINER)	0.93 ± 0.65	0.35 ± 0.24	79.56%	11.53	0.50	42.83	251 ± 88
SDSS J1447+4023	0.13025	MIRONG(LINER)	0.49 ± 0.14	0.37 ± 0.05	73.95%	12.39	1.26	43.57	245 ± 76
SDSS J1524+5314	0.08513	MIRONG(SF)	0.54 ± 0.26	0.36 ± 0.09	70.91%	13.40	1.08	42.73	246 ± 86
SDSS J0842+2357	0.06353	MIRONG(SF)	–	0.74 ± 0.11	–	12.80	0.81	42.60	< 154
SDSS J1549+3327	0.08565	MIRONG(SF)	–	0.75 ± 0.03	–	12.68	2.21	43.17	< 160
WTP14adbjsh	0.0106	WTP(Gold)	–	0.74 ± 0.03	–	7.99	2.10	43.17	< 182

**Figure 10.** MIR properties of the WTP sample. The upper panel shows $m_{\min, W2}$ and $\delta W2$, and the lower panel shows $L_{\max, W2}$ and t_{rise} . The gold and silver subsamples are shown in red and blue symbols. The meanings of symbols (dot, cross and inverted triangle) are the same as Figure 3.

According to the analysis of optically selected samples, the MIR emission of TDEs generally has a shorter rise time t_{rise} than CLAGNs. In particular, the two objects (AT 2017gge and AT 2018dyk) whose CVRs can not be measured due to too short t_{rise} are TDE/ANT instead of CLAGN. This suggests that objects with short t_{rise} have a high probability of being TDE/ANT. Thus, we selected three MIR outbursts hosted in non-Seyfert galaxies whose t_{rise} is shorter than the WISE sampling interval. Their MIR information is also listed in Table 3.

**Figure 11.** The distribution of ICs and CVRs of the WTP sample. Red and blue represent the gold and silver subsamples, respectively.

The MIR luminosities $L_{\max, W2}$ of these 11 TDE candidates are in the range of $\sim 10^{42.6} - 10^{43.6}$ erg s $^{-1}$, similar with optical TDEs with bright MIR emission. The rise times t_{rise} are generally less than 1 year, shorter than optical TDEs on average. This might be due to a selection effect, as we found a possible trend that TDEs with shorter rise times have larger CVRs. For example, the two optical TDEs with the largest CVRs which can pass the p_U criterion, including AT 2019dsg ($t_{\text{rise}} = 251 \pm 95$ day, $\text{CVR} = 0.66 \pm 0.15$) and AT 2020nov ($t_{\text{rise}} = 262 \pm 75$ day, $\text{CVR} = 0.74 \pm 0.23$), also have short rise time. However, the sample size is not large enough to confirm this trend.

6. DISCUSSIONS

6.1. Robustness of our method for distinguishing TDEs/ANTs and CLAGNs

6.1.1. Possible systematic errors

We had developed a new method to distinguish TDEs/ANTs from CLAGNs using MIR color variation

in the rising phase. In this subsection we discussed the uncertainties of the method.

The systematic errors of CVR measurement may come from the following aspects. First, the K-correction of the MIR color has a systematic error of $\sigma_{\text{sys}} = 0.04z$ mag due to uncertain SEDs, as estimated in Appendix B. Most of the objects in the samples in this work are at redshifts below 0.2, leading to systematic errors of $\lesssim 0.08$ mag. Secondly, our simulations indicate that the difference in sampling time may lead to a scatter in measured CVR of 0.02–0.15 mag yr⁻¹ (standard deviation) for the same MIR outburst, as shown in Figure 6, 7, E1 and E2. Finally, for a small fraction of MIR outbursts with poor data quality, some data points in the rising phase may not be included when calculating CVR because they do not meet the 3σ criterion in the W1 or W2 band.

The above systematic errors caused the CVR errors we gave to underestimate the actual uncertainty. Fortunately, the systematic errors should not significantly affect our main results. For most objects, the statistical errors are larger than the systematic errors and dominate the total errors. Moreover, as we demonstrated in section 3, measurement errors make the CVR distribution of a sample more diffused and blur the CVR distinctions between samples. Therefore, underestimating measurement error does not invalidate the conclusion that there is a CVR difference between TDEs/ANTs and CLAGNs based on optical samples, nor does it affect the reliability of CVR thresholds to divide regions.

Our conclusions and methods rely on the optical sample containing 13 TDE+ANTs and 19 CLAGNs. We cannot rule out the existence of “anomalies” whose CVRs deviate significantly from the usual parameter range of the sample. Considering these possible anomalies, high p_U (p_L) alone does not necessarily mean that a MIR outburst is TDE/ANT (CLAGN). For example, we considered the probability $p(\text{TA}|U)$ that an object with CVR falling in the U region is TDE/ANT according to Bayes’ equation:

$$p(\text{TA}|U) = \frac{f_{\text{TA}}p(U|\text{TA})}{f_{\text{TA}}p(U|\text{TA}) + f_{\text{CLAGN}}p(U|\text{CLAGN})}, \quad (7)$$

where f_{TA} and $f_{\text{CLAGN}} = 1 - f_{\text{TA}}$ are the fractions of TDE/ANT and CLAGN in the MIR outburst sample, respectively, and $p(U|\text{TA})$ or $p(U|\text{CLAGN})$ is the probability that the CVR of a TDE/ANT or CLAGN falls in the U region. We adopted a $p(U|\text{TA})$ value of 7/13 based on the observed CVRs of optical TDE+ANTs, and constrained $p(U|\text{CLAGN})$, the fraction of anomalies in CLAGNs, to be less than 1/19 based on the number of optical CLAGNs. Provided that the amounts of

TDE+ANTs and CLAGNs in MIR outbursts are comparable (f_{TA} in the range of 0.3–0.8, see section 6.2), $p(\text{TA}|U)$ is higher than 82%–98%. Based on a similar analysis, the probability that an object with CVR falling in the L region is CLAGN is higher than 77%–95%. Therefore, considering possible anomalies leads to a slight decrease in the probability that an outburst with high p_U (p_L) is TDE/ANT (CLAGN).

6.1.2. Comparison with diagnoses from other bands

We tested our method for distinguishing TDEs, ANT, and CLAGNs by comparing our classifications for MIR outbursts with diagnoses using data from other bands in the literature.

Wang et al. (2022a, hereafter Wang22) carried out follow-up optical spectral monitoring of 22 MIR outbursts in the MIRONG sample and diagnosed their nature. We ignored two optical TDEs and one optical CLAGN, and of the remaining 19 MIR outbursts, 10 are in non-Seyfert galaxies, and nine are in Seyfert galaxies. We selected four MIR outbursts with a short rise time or $p_U > 70\%$ as promising TDEs/ANTs (two TDEs in non-Seyfert galaxies and two ANT in Seyfert galaxies), and two with $p_L > 70\%$ as promising CLAGNs. They are listed in Table 4.

We compared our diagnoses with those by Wang22, which are also listed in Table 4. We found that except for some differences in terms (for example, we referred to TDE-like flares in AGNs as ANT without distinguishing their natures), only one out of the six was classified differently: J1043+2716 was classified as CLAGN with $\gtrsim 75\%$ confidence by us while classified as a TDE by Wang22 due to its declining broad emission lines and the presence of iron coronal lines. The MIR outburst J1043+2716 was first detected in May 2015, and the optical outburst must have begun earlier. Wang22’s classification relied on four spectra taken between April 2017 and March 2021, $\sim 2 - 5$ years after the outburst began. Without early-time spectra, the possibility of CLAGN cannot be ruled out by declining broad emission lines. In addition, strong iron coronal emission lines are also detected in AGNs (Clark et al. 2024), so the possibility of CLAGN cannot be fully ruled out by coronal lines. Besides, the probabilities of our promising TDE candidates are not high enough, and there may be individual sources that were misclassified. Therefore, the conflict between our and Wang22’s classification of J1043+2716 could be reconciled.

X-ray spectra are a reliable basis for distinguishing between TDEs and CLAGNs: many TDEs have soft spectra with steep spectral indices $\Gamma > 2$ (e.g., Saxton et al. 2020). In contrast, AGNs have relatively hard

Table 4. Comparison of our and literature diagnoses of MIR outbursts

Object	Our	Notes	Literature	Literature notes
Wang et al. (2022a) non-Seyfert				
J1513+3111	TDE	CVR = 0.65 ± 0.22 , $p_U = 86.1\%$	TDE	declining, iron CL, He II, N III
J1549+3327	TDE	$t_{\text{rise}} < 160$ day	TDE	declining, iron CL, He II
J1043+2716	CLAGN	CVR = 0.04 ± 0.09 , $p_L = 74.9\%$	TDE	declining, iron CL
J1442+5558	CLAGN	CVR = 0.00 ± 0.12 , $p_L = 80.6\%$	turn-on	maintain, iron CL, He II, N III
Wang et al. (2022a) Seyfert				
J1332+2036	ANT	CVR = 1.00 ± 0.12 , $p_U = 100\%$	AGN flare	declining
J1402+3922	ANT	CVR = 1.08 ± 0.18 , $p_U = 100\%$	TDE	restored, iron CL, He II
Masterson et al. (2024) with X-ray				
WTP 17aamoxe	TDE	CVR = 0.88 ± 0.07 , $p_U = 100\%$	TDE	soft X-ray with $\Gamma = 3.8^{+1.4}_{-1.9}$
WTP 17aamzew	unsure	CVR = 0.28 ± 0.22	TDE	soft X-ray with $\Gamma = 4.1^{+2.3}_{-1.8}$

spectra with $\Gamma \lesssim 2$ (e.g., Piconcelli et al. 2005). In the WTP sample, three MIR outbursts were detected in the X-ray band by eROSITA after they occurred. Based on soft and steep X-ray spectra, Masterson et al. (2024) identified two likely TDEs, whose information is listed in Table 4. Of these two X-ray-verified TDEs, WTP 17aamoxe is also identified as likely TDE by us because it falls in the U region with 100% probability, and WTP 17aamzew has a CVR of 0.28 ± 0.22 , also consistent with the TDE interpretation. Therefore, our classifications for the WTP sample agree with the X-ray diagnoses.

6.2. Fractions of TDEs, ANTs and CLAGNs in MIR selected samples

In sections 5.1 and 5.2, we estimated the lower limits of the numbers of TDEs, ANTs and CLAGN using the numbers in the U and L regions for MIRONG and WTP samples. However, the numbers do not include objects in the M region, where individual objects could not be reliably classified. Nevertheless, we could estimate the numbers of TDEs, ANTs and CLAGNs in the M region by using the probabilities of these types of outbursts falling in the M region.

For the eight optical TDEs, six have CVRs in the U region, and two have CVRs in the M region. Assuming that the fraction of TDEs in the U region $f_{U,\text{TDE}}$ has a uniform prior distribution between 0 and 1, and the observed number obeys the binomial distribution, we calculated a posterior distribution using Bayes' method. Using the posterior distribution, we obtained $f_{U,\text{TDE}} = 0.71^{+0.13}_{-0.16}$ and $f_{M,\text{TDE}} = 1 - f_{U,\text{TDE}} = 0.29^{+0.16}_{-0.13}$. In a similar way, we obtained $f_{U,\text{ANT}} = 0.32^{+0.17}_{-0.14}$, $f_{M,\text{ANT}} = 0.68^{+0.14}_{-0.17}$, $f_{L,\text{CLAGN}} = 0.57 \pm 0.11$, and $f_{M,\text{CLAGN}} = 0.43 \pm 0.11$.

For the MIRONG non-Seyfert sample with $N_U = 23$, $N_M = 27$ and $N_L = 18$, we assumed that the number of TDEs in the U region is N_U and the number of CLAGNs

in the L region is N_L . Then, the numbers of TDEs and CLAGNs in the M region satisfy $N_{M,\text{TDE}} = N_U \times \frac{f_{M,\text{TDE}}}{f_{U,\text{TDE}}}$ and $N_{M,\text{CLAGN}} = N_L \times \frac{f_{M,\text{CLAGN}}}{f_{L,\text{CLAGN}}}$. Thus, their probability density distributions are:

$$\begin{aligned} \frac{dp(N_{M,\text{TDE}})}{dN_{M,\text{TDE}}} &= \frac{dp(f_{U,\text{TDE}})}{df_{U,\text{TDE}}} \frac{f_{U,\text{TDE}}^2}{N_U} \\ \frac{dp(N_{M,\text{CLAGN}})}{dN_{M,\text{CLAGN}}} &= \frac{dp(f_{L,\text{CLAGN}})}{df_{L,\text{CLAGN}}} \frac{f_{L,\text{CLAGN}}^2}{N_L} \end{aligned} \quad (8)$$

With the constraint equation $N_{M,\text{TDE}} + N_{M,\text{CLAGN}} = N_M$, we calculated the posterior probability distributions of $N_{M,\text{TDE}}$ and $N_{M,\text{CLAGN}}$ using Bayes' equation. The results show that $N_{M,\text{TDE}} = 11.3 \pm 5.1$ and $N_{M,\text{CLAGN}} = 15.7 \pm 5.1$. In a similar way, we obtained $N_{M,\text{ANT}} = 7.7 \pm 2.7$ and $N_{M,\text{CLAGN}} = 9.3 \pm 2.7$ for the MIRONG Seyfert sample, and $N_{M,\text{TDE}} = 8.0^{+0.9}_{-1.8}$ and $N_{M,\text{CLAGN}} = 2.0^{+1.8}_{-0.9}$ for the WTP sample.

We then considered the MIR outbursts that were excluded during the selection of the rising phase. There are two cases: one is that the t_{rise} is too short to calculate CVR, and the other is that the outburst starts at the first data point of NEOWISE-R. We assumed that outbursts in the former case are all TDEs/ANTs. The outbursts in the latter case could not be classified using color variation, so they are either TDE/ANT or CLAGN. With these outbursts included, we estimated the fractions of TDEs/ANTs and CLAGNs in the MIR outburst samples, and the results are listed in Table 5.

The results confirmed our conclusion in section 5 that all MIR outburst samples are mixtures of TDEs/ANTs and CLAGNs. Overall, MIR outbursts consist of comparable amounts of TDEs/ANTs and CLAGNs: more than half in non-Seyfert galaxies are TDEs, and more than half in Seyfert galaxies are CLAGNs.

Can CLAGNs occur in non-Seyfert galaxies? Non-Seyfert galaxies were selected using narrow-line-ratio

Table 5. Fractions of TDEs/ANTs in the MIR outburst samples.

	f_{TDE}	f_{ANT}	f_{CLAGN}
non-Seyfert (77)	45%–63%	-	37%–55%
Seyfert (50)	-	30%–57%	43%–70%
WTP (18)	62%–82%	-	18%–38%

and MIR color diagnoses (Jiang et al. 2021; Masterson et al. 2024). These diagnoses cannot fully rule out weak AGNs whose signals are overwhelmed by star formation. Thus, for the outbursts in the MIRONG and WTP non-Seyfert samples that were diagnosed as CLAGNs by MIR color, their host galaxies may have weak AGNs, even though there was no clear AGN signal before the outbursts.

The fraction of TDEs in the WTP sample (62%–82%) is higher than that in the MIRONG non-Seyfert sample (45%–63%). This is possibly because Masterson et al. (2024) required an additional criterion that the MIR LC must have a fast rise and a slow, monotonic decay. However, CLAGNs could not be completely excluded after adding this criterion, as the fraction of CLAGNs in the WTP sample is still $\gtrsim 20\%$, possibly because some CLAGNs also meet this criterion. In addition, it is likely that some TDEs, for example, AT 2019qiz (Figure A2) whose MIR emission rises nonmonotonically in > 925 days, fail to pass this criterion. Therefore, this standard may improve the purity of TDEs while losing completeness.

6.3. Implications and future works

Jiang et al. (2021) and Masterson et al. (2024) obtained incident rates of MIR outbursts with their samples of 5.4×10^{-5} and $2.0 \pm 0.3 \times 10^{-5}$ galaxy $^{-1}$ yr $^{-1}$, respectively. We estimated the incident of IR TDEs using their results and our estimations of the TDE fractions. For the MIRONG sample, with the 77 MIR outbursts in non-Seyfert galaxies that are not supernovae and are radio-quiet, we could estimate a rate of 3.4×10^{-5} galaxy $^{-1}$ yr $^{-1}$ considering that non-Seyfert galaxies make up $\sim 90\%$ of SDSS galaxies (Kewley et al. 2006). Assuming that 45%–63% of them are TDEs, the incident rate of IR TDEs is $1.5 - 2.1 \times 10^{-5}$ galaxy $^{-1}$ yr $^{-1}$. For the WTP sample, Masterson et al. (2024) estimated the rate using 12 MIR outbursts in their gold sample. According to our estimation, 62%–82% of their total 18 outbursts are TDEs, and hence the rate should be modified to $1.6 - 2.8 \times 10^{-5}$ galaxy $^{-1}$ yr $^{-1}$, which is consistent with the rate Masterson et al. (2024) derived using only their gold sample. Therefore, the results from

the MIRONG and WTP samples are consistent, and the final rate is $1.5 - 2.8 \times 10^{-5}$ galaxy $^{-1}$ yr $^{-1}$, comparable with the optical TDE rate of $3.2_{-0.6}^{+0.8} \times 10^{-5}$ galaxy $^{-1}$ yr $^{-1}$ (Yao et al. 2023) within the margin of error.

Part of IR TDEs are bright in both optical and IR bands and are also included in optical TDEs. Jiang et al. (2021) and Masterson et al. (2024) estimated optical detections for MIR outbursts of 11% and 22%, respectively. In addition, of the 33 optical TDEs in Yao et al. (2023), only two (AT 2019dsg and AT 2019qiz) are MIR bright. Thus, there is not much overlap between optical TDEs and IR TDEs. Combining results from optical, X-ray and IR surveys, we estimated a total TDE rate of $\sim 5 - 8 \times 10^{-5}$ galaxy $^{-1}$ yr $^{-1}$.

So far, our method has not been able to classify most of the MIR outbursts clearly, mainly due to the large measurement errors of MIR colors and the semi-annual sampling interval of the WISE project, which is not frequent enough. Nevertheless, some MIR outbursts can already be classified based on the available data. For example, SDSS J154843.06+220812.6, whose radio counterpart VT J154843.06+220812.6 has been studied in detail by Somalwar et al. (2022), is a likely CLAGN because of its CVR of -0.08 ± 0.03 , corresponding a p_L of 100%.

Although the WISE telescope was retired in July 2024, the Near-Earth Object Surveyor (Mainzer et al. 2023) will launch in 2027. Furthermore, there will be some wide-field NIR survey projects in the future, such as the wide-field infrared transient explorer (WINTER, Lourie et al. 2020), PRime-focus Infrared Microlensing Experiment (PRIME, Kondo et al. 2023), and the Nancy Grace Roman Space Telescope (Akeson et al. 2019). These projects will discover a large amount of IR outbursts in galaxy centers, and obtain their high-quality, high-cadence NIR LCs. Our simulations predict that the NIR color $H - K$ of TDEs also turns red faster in the rising phase than CLAGNs, with a pattern similar to MIR color (Appendix E.3). If true, IR outbursts can also be classified based on the NIR CVR. Due to the high quality and cadence of NIR data, we expected to obtain more IR outbursts with precise classification by the NIR CVR.

We have found that the rise times and variability amplitudes of TDEs and CLAGNs are also different on average. Although it is difficult to distinguish TDEs and CLAGNs using each parameter itself, by combining all the parameters with the help of machine learning, the accuracy of classification may be improved.

The classification based on CVR has a unique advantage in that a preliminary diagnosis can be obtained using only the rising phase of the LC. This allows one

to select likely TDEs or exclude likely CLAGNs in the early phases of IR outbursts and is further convenient for timely multi-band follow-up observations.

7. SUMMARY AND CONCLUSIONS

In this work, we selected MIR-bright optical outbursts, including 9 TDEs, 8 ANTs and 19 CLAGNs. Using the WISE MIR LCs sampled every half a year since 2014 in W1 and W2 bands, we calculated the K-corrected W1-W2 color in the rising phase and investigated its time variation.

We found that the MIR color of TDEs and ANTs generally turns red quickly during the rising phase, while CLAGN generally does not. Quantitatively, the median CVR of TDEs and ANTs is $\sim 0.4 \text{ mag yr}^{-1}$, higher than that of CLAGNs of 0.09 mag yr^{-1} . The CVR distributions of TDEs and ANTs differ from that of CLAGNs by significances of 2.9×10^{-5} and 3.1×10^{-4} , respectively, estimated using K-S tests. In addition, the initial MIR color of TDEs is generally redder than that of ANTs, as the median ICs of TDEs and ANTs are 0.52 and 0.36 mag, respectively, which differ by a significance of 0.020.

Using simulations involving the dust radiative transfer model, we explored the origins of the two phenomena. The MIR color of TDEs and ANTs turning red quickly possibly results from their UV LCs characterized by “rapid rise, short peak and long tail”. In addition, the difference in IC between TDEs and ANTs may be related to the difference in the geometry of the echoing dust: the dust structure around TDEs is approximately spherically symmetric, while that around ANTs has a torus shape with face-on inclination.

We proposed a method to classify MIR outbursts based on the CVR difference between TDEs/ANTs and CLAGNs. We divided three regions: a U region with CVR greater than 0.4 mag yr^{-1} representing a high probability of being TDE/ANT, an L region with CVR less than 0.1 mag yr^{-1} representing a high probability of being CLAGN, and an M region between them, where the outbursts are difficult to classify. In addition, MIR outbursts with a rise time shorter than half a year have a high probability of being TDEs/ANTs, because the two optical outbursts that meet this condition are TDE/ANT.

Using this method, we classified 127 MIR outbursts in the MIRONG sample of Jiang et al. (2021) and 18 in the WTP sample of Masterson et al. (2024). For the MIRONG sample, we divided it into a non-Seyfert subsample and a Seyfert subsample, according to the types of host galaxies, containing 77 and 50 MIR outbursts, respectively. We found that in all three samples, both likely TDEs/ANTs and likely CLAGNs exist, and hence, they are all mixtures of TDEs/ANTs and CLAGNs. We selected 11 promising TDE candidates based on a high probability of CVR falling in the U region or a short rise time. We examined our classifications with those in the literature based on follow-up optical spectra and X-ray observations and found no apparent contradiction.

We inferred that 45%–63% of MIR outbursts are TDEs in the MIRONG non-Seyfert subsample, 30%–57% in the MIRONG Seyfert subsample are ANTs, 62%–82% in the WTP sample are TDEs, and the remainders are CLAGNs. Thus, MIR outbursts contain comparable amounts of TDEs/ANTs and CLAGNs overall, and those in non-Seyfert galaxies are mostly TDEs. Using the TDE fractions above, we estimated the incident rate of IR TDEs in non-Seyfert galaxies to be $1.5\text{--}2.8 \times 10^{-5} \text{ galaxy}^{-1} \text{ yr}^{-1}$ with the MIRONG and WTP samples, comparable with that of optical TDEs within the margin of error.

Although this work only studied the variation of MIR color, it is hopeful that the variation of NIR color can also be used to classify IR outbursts. We expect that more IR outbursts will be discovered and classified with future high-quality, high-cadence IR surveys. This will eventually shed new light on the statistical study of obscuring TDEs.

- 1 This work is supported by the National Natural Science
- 2 Foundation of China (NFSC, 12103002) and the Univer-
- 3 sity Annual Scientific Research Plan of Anhui Province
- 4 (2022AH010013, 2023AH030052). This publication
- 5 makes use of data products from NEOWISE, which is a
- 6 project of the Jet Propulsion Laboratory/California In-
- 7 stitute of Technology, funded by the Planetary Science
- 8 Division of the National Aeronautics and Space Admin-
- 9 istration.

REFERENCES

- Akeson, R., Armus, L., Bachelet, E., et al. 2019, arXiv e-prints, arXiv:1902.05569, doi: [10.48550/arXiv.1902.05569](https://doi.org/10.48550/arXiv.1902.05569)
- Antonucci, R. 1993, *ARA&A*, 31, 473, doi: [10.1146/annurev.aa.31.090193.002353](https://doi.org/10.1146/annurev.aa.31.090193.002353)
- Blanchard, P. K., Nicholl, M., Berger, E., et al. 2017, *ApJ*, 843, 106, doi: [10.3847/1538-4357/aa77f7](https://doi.org/10.3847/1538-4357/aa77f7)
- Brogan, R., Krumpke, M., Homan, D., et al. 2023, *A&A*, 677, A116, doi: [10.1051/0004-6361/202346475](https://doi.org/10.1051/0004-6361/202346475)

- Chen, J.-H., Dou, L.-M., & Shen, R.-F. 2022, *ApJ*, 928, 63, doi: [10.3847/1538-4357/ac558d](https://doi.org/10.3847/1538-4357/ac558d)
- Clark, P., Graur, O., Callow, J., et al. 2024, *MNRAS*, 528, 7076, doi: [10.1093/mnras/stae460](https://doi.org/10.1093/mnras/stae460)
- Clark, P., Callow, J., Graur, O., et al. 2025, arXiv e-prints, arXiv:2502.04080, doi: [10.48550/arXiv.2502.04080](https://doi.org/10.48550/arXiv.2502.04080)
- Cohen, R. D., Rudy, R. J., Puetter, R. C., Ake, T. B., & Foltz, C. B. 1986, *ApJ*, 311, 135, doi: [10.1086/164758](https://doi.org/10.1086/164758)
- Dodd, S. A., Nukala, A., Connor, I., et al. 2023, *ApJ*, 959, 19, doi: [10.3847/2041-8213/ad1112](https://doi.org/10.3847/2041-8213/ad1112)
- Earl, N., French, K. D., Ramirez-Ruiz, E., et al. 2024, arXiv e-prints, arXiv:2412.12991, doi: [10.48550/arXiv.2412.12991](https://doi.org/10.48550/arXiv.2412.12991)
- Frederick, S., Gezari, S., Graham, M. J., et al. 2019, *ApJ*, 883, 31, doi: [10.3847/1538-4357/ab3a38](https://doi.org/10.3847/1538-4357/ab3a38)
- Frederick, S., Gezari, S., Graham, M. J., et al. 2021, *ApJ*, 920, 56, doi: [10.3847/1538-4357/ac110f](https://doi.org/10.3847/1538-4357/ac110f)
- French, K. D., Arcavi, I., & Zabludoff, A. 2016, *ApJL*, 818, L21, doi: [10.3847/2041-8205/818/1/L21](https://doi.org/10.3847/2041-8205/818/1/L21)
- Guolo, M., Gezari, S., Yao, Y., et al. 2024, *ApJ*, 966, 160, doi: [10.3847/1538-4357/ad2f9f](https://doi.org/10.3847/1538-4357/ad2f9f)
- Hammerstein, E., van Velzen, S., Gezari, S., et al. 2023, *ApJ*, 942, 9, doi: [10.3847/1538-4357/aca283](https://doi.org/10.3847/1538-4357/aca283)
- Hinkle, J. T. 2024, *MNRAS*, 531, 2603, doi: [10.1093/mnras/stae1229](https://doi.org/10.1093/mnras/stae1229)
- Huang, S., Jiang, N., Lin, Z., Zhu, J., & Wang, T. 2023, *MNRAS*, 525, 4057, doi: [10.1093/mnras/stad2541](https://doi.org/10.1093/mnras/stad2541)
- Husemann, B., Urrutia, T., Tremblay, G. R., et al. 2016, *A&A*, 593, L9, doi: [10.1051/0004-6361/201629245](https://doi.org/10.1051/0004-6361/201629245)
- Jiang, N., Dou, L., Wang, T., et al. 2016, *ApJL*, 828, L14, doi: [10.3847/2041-8205/828/1/L14](https://doi.org/10.3847/2041-8205/828/1/L14)
- Jiang, N., Wang, T., Yan, L., et al. 2017, *ApJ*, 850, 63, doi: [10.3847/1538-4357/aa93f5](https://doi.org/10.3847/1538-4357/aa93f5)
- Jiang, N., Wang, T., Dou, L., et al. 2021, *ApJS*, 252, 32, doi: [10.3847/1538-4365/abd1dc](https://doi.org/10.3847/1538-4365/abd1dc)
- Kewley, L. J., Groves, B., Kauffmann, G., & Heckman, T. 2006, *MNRAS*, 372, 961, doi: [10.1111/j.1365-2966.2006.10859.x](https://doi.org/10.1111/j.1365-2966.2006.10859.x)
- Kondo, I., Sumi, T., Koshimoto, N., et al. 2023, *AJ*, 165, 254, doi: [10.3847/1538-3881/acccf9](https://doi.org/10.3847/1538-3881/acccf9)
- Kool, E. C., Reynolds, T. M., Mattila, S., et al. 2020, *MNRAS*, 498, 2167, doi: [10.1093/mnras/staa2351](https://doi.org/10.1093/mnras/staa2351)
- Kosec, P., Pasham, D., Kara, E., & Tombesi, F. 2023, *ApJ*, 954, 170, doi: [10.3847/1538-4357/aced87](https://doi.org/10.3847/1538-4357/aced87)
- Lourie, N. P., Baker, J. W., Burruss, R. S., et al. 2020, in *Society of Photo-Optical Instrumentation Engineers (SPIE) Conference Series*, Vol. 11447, *Ground-based and Airborne Instrumentation for Astronomy VIII*, ed. C. J. Evans, J. J. Bryant, & K. Motohara, 114479K, doi: [10.1117/12.2561210](https://doi.org/10.1117/12.2561210)
- Lu, K.-X., Li, Y.-R., Wu, Q., et al. 2025, *ApJS*, 276, 51, doi: [10.3847/1538-4365/ad9a5a](https://doi.org/10.3847/1538-4365/ad9a5a)
- Lu, W., Kumar, P., & Evans, N. J. 2016, *MNRAS*, 458, 575, doi: [10.1093/mnras/stw307](https://doi.org/10.1093/mnras/stw307)
- Lyu, B., Wu, Q., Yan, Z., Yu, W., & Liu, H. 2022, *ApJ*, 927, 227, doi: [10.3847/1538-4357/ac5256](https://doi.org/10.3847/1538-4357/ac5256)
- Mainzer, A., Bauer, J., Cutri, R. M., et al. 2014, *ApJ*, 792, 30, doi: [10.1088/0004-637X/792/1/30](https://doi.org/10.1088/0004-637X/792/1/30)
- Mainzer, A. K., Masiero, J. R., Abell, P. A., et al. 2023, *PSJ*, 4, 224, doi: [10.3847/PSJ/ad0468](https://doi.org/10.3847/PSJ/ad0468)
- Makrygianni, L., Trakhtenbrot, B., Arcavi, I., et al. 2023, *ApJ*, 953, 32, doi: [10.3847/1538-4357/ace1ee](https://doi.org/10.3847/1538-4357/ace1ee)
- Malyali, A., Rau, A., Merloni, A., et al. 2021, *A&A*, 647, A9, doi: [10.1051/0004-6361/202039681](https://doi.org/10.1051/0004-6361/202039681)
- Masterson, M., De, K., Panagiotou, C., et al. 2024, *ApJ*, 961, 211, doi: [10.3847/1538-4357/ad18bb](https://doi.org/10.3847/1538-4357/ad18bb)
- Mattila, S., Pérez-Torres, M., Efstathiou, A., et al. 2018, *Science*, 361, 482, doi: [10.1126/science.aao4669](https://doi.org/10.1126/science.aao4669)
- Meisner, A. M., Lang, D., & Schlegel, D. J. 2018, *AJ*, 156, 69, doi: [10.3847/1538-3881/aacbcd](https://doi.org/10.3847/1538-3881/aacbcd)
- Necker, J., Graikou, E., Kowalski, M., et al. 2024, arXiv e-prints, arXiv:2407.01039, doi: [10.48550/arXiv.2407.01039](https://doi.org/10.48550/arXiv.2407.01039)
- Nenkova, M., Sirocky, M. M., Nikutta, R., Ivezić, Ž., & Elitzur, M. 2008, *ApJ*, 685, 160, doi: [10.1086/590483](https://doi.org/10.1086/590483)
- Neustadt, J. M. M., Holoiën, T. W. S., Kochanek, C. S., et al. 2020, *MNRAS*, 494, 2538, doi: [10.1093/mnras/staa859](https://doi.org/10.1093/mnras/staa859)
- Newsome, M., Arcavi, I., Howell, D. A., et al. 2024, *ApJ*, 977, 258, doi: [10.3847/1538-4357/ad8a69](https://doi.org/10.3847/1538-4357/ad8a69)
- Onori, F., Cannizzaro, G., Jonker, P. G., et al. 2022, *MNRAS*, 517, 76, doi: [10.1093/mnras/stac2673](https://doi.org/10.1093/mnras/stac2673)
- Peterson, B. M. 1997, *An Introduction to Active Galactic Nuclei*
- Petrushevskaya, T., Leloudas, G., Ilić, D., et al. 2023, *A&A*, 669, A140, doi: [10.1051/0004-6361/202244623](https://doi.org/10.1051/0004-6361/202244623)
- Piconcelli, E., Jimenez-Bailón, E., Guainazzi, M., et al. 2005, *A&A*, 432, 15, doi: [10.1051/0004-6361:20041621](https://doi.org/10.1051/0004-6361:20041621)
- Rees, M. J. 1988, *Nature*, 333, 523, doi: [10.1038/333523a0](https://doi.org/10.1038/333523a0)
- Reynolds, T. M., Mattila, S., Efstathiou, A., et al. 2022, *A&A*, 664, A158, doi: [10.1051/0004-6361/202243289](https://doi.org/10.1051/0004-6361/202243289)
- Ricci, C., & Trakhtenbrot, B. 2023, *Nature Astronomy*, 7, 1282, doi: [10.1038/s41550-023-02108-4](https://doi.org/10.1038/s41550-023-02108-4)
- Saxton, R., Komossa, S., Auchettl, K., & Jonker, P. G. 2020, *SSRv*, 216, 85, doi: [10.1007/s11214-020-00708-4](https://doi.org/10.1007/s11214-020-00708-4)
- Sazonov, S., Gilfanov, M., Medvedev, P., et al. 2021, *MNRAS*, 508, 3820, doi: [10.1093/mnras/stab2843](https://doi.org/10.1093/mnras/stab2843)
- Shappee, B. J., Prieto, J. L., Grupe, D., et al. 2014, *ApJ*, 788, 48, doi: [10.1088/0004-637X/788/1/48](https://doi.org/10.1088/0004-637X/788/1/48)

- Sheng, Z., Wang, T., Jiang, N., et al. 2017, *ApJL*, 846, L7, doi: [10.3847/2041-8213/aa85de](https://doi.org/10.3847/2041-8213/aa85de)
- Somalwar, J. J., Ravi, V., Dong, D., et al. 2022, *ApJ*, 929, 184, doi: [10.3847/1538-4357/ac5e29](https://doi.org/10.3847/1538-4357/ac5e29)
- Sun, L., Jiang, N., Wang, T., et al. 2020, *ApJ*, 898, 129, doi: [10.3847/1538-4357/ab9f2c](https://doi.org/10.3847/1538-4357/ab9f2c)
- Trakhtenbrot, B., Arcavi, I., Ricci, C., et al. 2019, *Nature Astronomy*, 3, 242, doi: [10.1038/s41550-018-0661-3](https://doi.org/10.1038/s41550-018-0661-3)
- van Velzen, S., Holoien, T. W. S., Onori, F., Hung, T., & Arcavi, I. 2020, *SSRv*, 216, 124, doi: [10.1007/s11214-020-00753-z](https://doi.org/10.1007/s11214-020-00753-z)
- van Velzen, S., Mendez, A. J., Krolik, J. H., & Gorjian, V. 2016, *ApJ*, 829, 19, doi: [10.3847/0004-637X/829/1/19](https://doi.org/10.3847/0004-637X/829/1/19)
- van Velzen, S., Gezari, S., Hammerstein, E., et al. 2021, *ApJ*, 908, 4, doi: [10.3847/1538-4357/abc258](https://doi.org/10.3847/1538-4357/abc258)
- Veres, P. M., Franckowiak, A., van Velzen, S., et al. 2024, arXiv e-prints, arXiv:2408.17419, doi: [10.48550/arXiv.2408.17419](https://doi.org/10.48550/arXiv.2408.17419)
- Wang, Y., Jiang, N., Wang, T., et al. 2022a, *ApJS*, 258, 21, doi: [10.3847/1538-4365/ac33a6](https://doi.org/10.3847/1538-4365/ac33a6)
- . 2022b, *ApJL*, 930, 4, doi: [10.3847/2041-8213/ac6670](https://doi.org/10.3847/2041-8213/ac6670)
- Wang, Y., Wang, T., Jiang, N., et al. 2024, *ApJ*, 966, 136, doi: [10.3847/1538-4357/ad2ae4](https://doi.org/10.3847/1538-4357/ad2ae4)
- Wang, Y., Pasham, D. R., Altamirano, D., et al. 2024, *ApJ*, 962, 78, doi: [10.3847/1538-4357/ad182b](https://doi.org/10.3847/1538-4357/ad182b)
- Wiseman, P., Williams, R. D., Arcavi, I., et al. 2025, *MNRAS*, 537, 2024, doi: [10.1093/mnras/staf116](https://doi.org/10.1093/mnras/staf116)
- Wright, E. L., Eisenhardt, P. R. M., Mainzer, A. K., et al. 2010, *AJ*, 140, 1868, doi: [10.1088/0004-6256/140/6/1868](https://doi.org/10.1088/0004-6256/140/6/1868)
- Yan, L., Wang, T., Jiang, N., et al. 2019, *ApJ*, 874, 44, doi: [10.3847/1538-4357/ab074b](https://doi.org/10.3847/1538-4357/ab074b)
- Yang, Q., Wu, X.-B., Fan, X., et al. 2018, *ApJ*, 862, 109, doi: [10.3847/1538-4357/aaca3a](https://doi.org/10.3847/1538-4357/aaca3a)
- Yao, Y., Margutti, R., & Qin, Y. 2023, *Transient Name Server AstroNote*, 273, 1. <https://ui.adsabs.harvard.edu/abs/2023TNSAN.273....1Y>
- Yao, Y., Ravi, V., Gezari, S., et al. 2023, *ApJL*, 955, L6, doi: [10.3847/2041-8213/acf216](https://doi.org/10.3847/2041-8213/acf216)
- Zabludoff, A., Arcavi, I., LaMassa, S., et al. 2021, *SSRv*, 217, 54, doi: [10.1007/s11214-021-00829-4](https://doi.org/10.1007/s11214-021-00829-4)
- Zhang, Z., Shu, X., Yang, L., et al. 2025, arXiv e-prints, arXiv:2501.08812, doi: [10.48550/arXiv.2501.08812](https://doi.org/10.48550/arXiv.2501.08812)

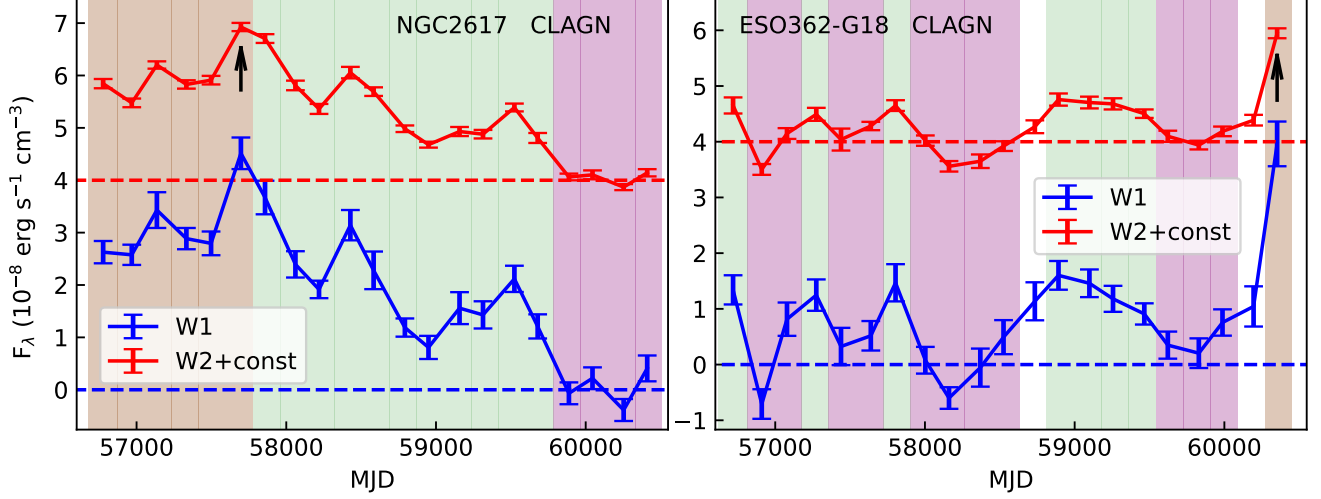


Figure A1. The MIR LCs, the selections of quiescent, outburst states and rising phase of NGC 2617 and ESO362-G18. The meaning of labels and colors are the same as Figure 1(b).

APPENDIX

A. DISPLAY OF SPECIAL OBJECTS

Here, we show the information of the eight CLAGNs excluded in section 2.3 and demonstrate why we excluded them. For seven CLAGNs, including 3C 390.3, HE1136-2304, Mrk 6, Mrk 926, NGC 2617, NGC 4395, and SDSS J080020.98+263648.8, the outburst started in the first data point of NEOWISE-R, which are typically between December 2013 and June 2014. We show an example NGC 2617 (Figure A1(a)), for which our algorithm identified an outburst from 2014 to 2022. However, the outburst started earlier than April 2013 (Shappee et al. 2014). Therefore, it is likely that NEOWISE-R observations missed the beginning of the outburst for the seven CLAGNs. For one CLAGN, ESO 362-G18 (Figure A1(b)), the outburst started too late, and only one data point can be used in the rising phase. The color variation rate in the rising phase can not be calculated, so we removed it.

In addition, we display the MIR LCs of TDE AT 2017gge and ANT AT 2018bcb with short rise time, and that of TDE AT 2019qiz with long rise time.

B. K-CORRECTION FOR THE MIR COLOR

The color $C = W1 - W2$ of a target in the observer's frame is determined by SED and redshift. We considered three types of SEDs: blackbody, optically thin graphite, and silicate. The blackbody SED is expressed as:

$$L_{\lambda}(\lambda) = \pi B_{\lambda}(\lambda, T_{\text{BB}}) 4\pi r_{\text{BB}}^2, \quad (\text{B1})$$

where B_{λ} is the Planck function, T_{BB} and r_{BB} are the blackbody temperature and blackbody radius, respectively. The SED of optically thin graphite or silicate can be expressed as:

$$L_{\lambda}(\lambda) = 4\pi B_{\lambda}(\lambda, T_d) M_d \kappa_{\lambda}(a), \quad (\text{B2})$$

where T_d and M_d are the temperature and mass of the dust, and $\kappa_{\lambda}(a)$ is the dust mass absorption coefficient for grain radius a . We adopted the absorption coefficients from Laor & Draine (1993) and converted them to κ_{λ} following Fox et al. (2010).

Using the SEDs, we predicted the color C for a given redshift z as:

$$C(z) = -2.5 \text{Log} \left[\frac{\int_0^{\infty} f_{\lambda}(\frac{\lambda}{1+z}) S_{W1}(\lambda) d\lambda}{\int_0^{\infty} f_{\lambda}(\frac{\lambda}{1+z}) S_{W2}(\lambda) d\lambda} \frac{f_{0,W2}}{f_{0,W1}} \right], \quad (\text{B3})$$

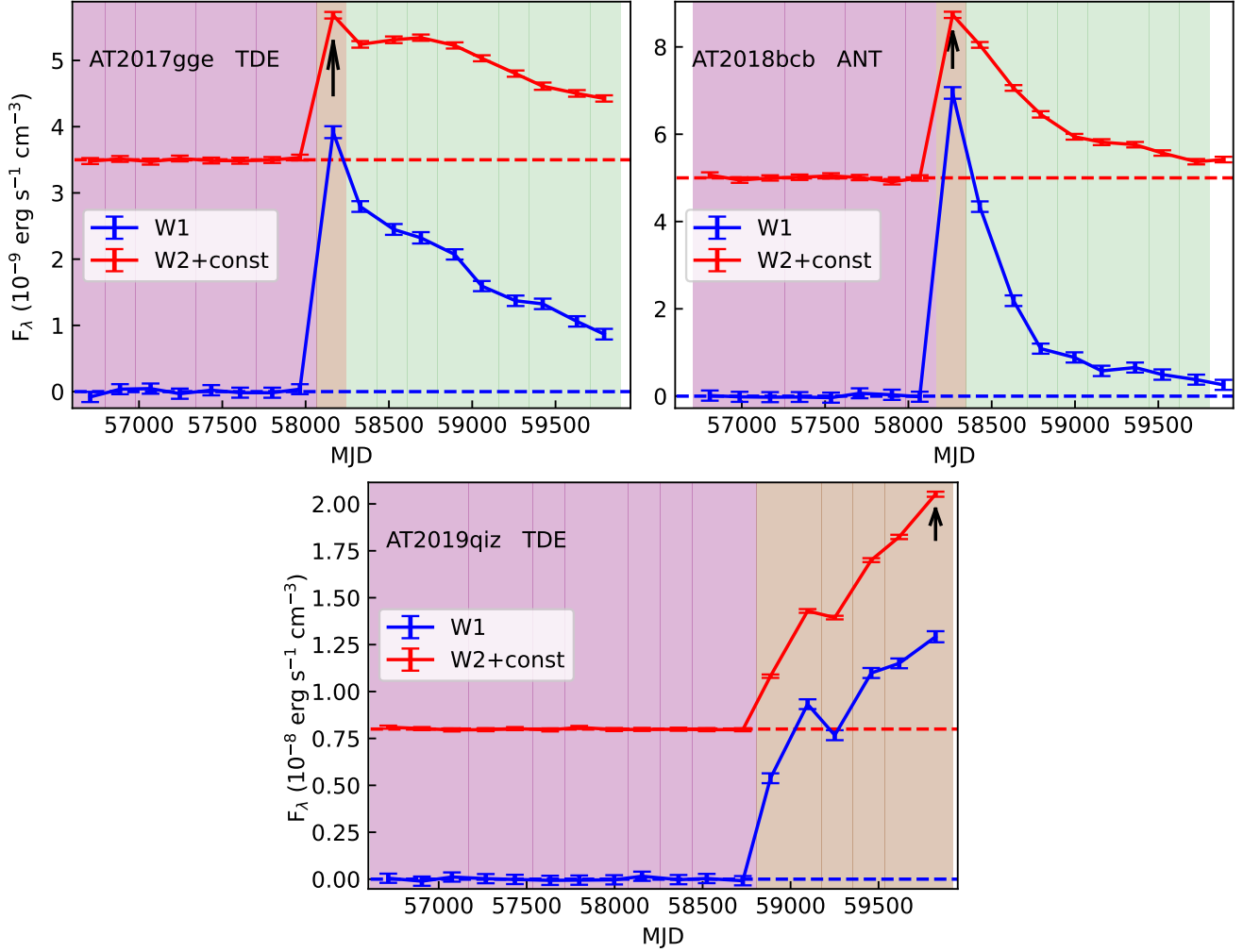


Figure A2. The MIR LCs, the selections of quiescent, outburst states and rising phase of AT 2017gge, AT 2018bcb and AT 2019qiz. The meaning of labels and colors are the same as Figure 1(b).

where $S_{W1}(\lambda)$ and $S_{W2}(\lambda)$ are the normalized transmission curves of the WISE W1 and W2 filters⁵, and $f_{0,W1}$ and $f_{0,W2}$ are the zero points of the two filters.

In Figure B1(a), we show the relationships between rest-frame colors and temperature for different SEDs. The results for grain radius $a = 0.0316, 0.01$ and $0.316 \mu\text{m}$ are displayed for optically thin graphite and silicate. At the same temperature, graphite dust is the bluest, followed by silicate dust, and blackbody is the reddest. The color of actual dust may be more complex. If the dust is a mixture of graphite and silicate, the color would be between pure graphite and silicate. In addition, if the MIR optical depth of the dust is on the order of magnitude of 1, the color would be between those of optically thin dust and blackbody. Therefore, despite the complexity of the SED of actual dust, its color can still be constrained by the above simple SED models.

For different redshifts, temperatures, and types of SEDs, we calculated K-correction $K(z) = C(z) - C(0)$, where $C(z)$ and $C(0)$ are colors in the observer's frame and the rest frame, respectively. We show the $K(z)$ as a function of $C(z)$ for $z = 0.1$ in Figure B1(b). We found that the functions assuming different types of SEDs are approximately a series of parallel lines. For $z < 0.35$, the top is always graphite with $a = 0.316 \mu\text{m}$, and the bottom is always the blackbody. Therefore, we adopted the average of the $K(z)$ given by these two types of SEDs as the final K-correction curve (the black line), and estimated the systematic error by half of their difference. The final K-corrections and the

⁵ https://wise2.ipac.caltech.edu/docs/release/prelim/expsup/sec4_3g.html

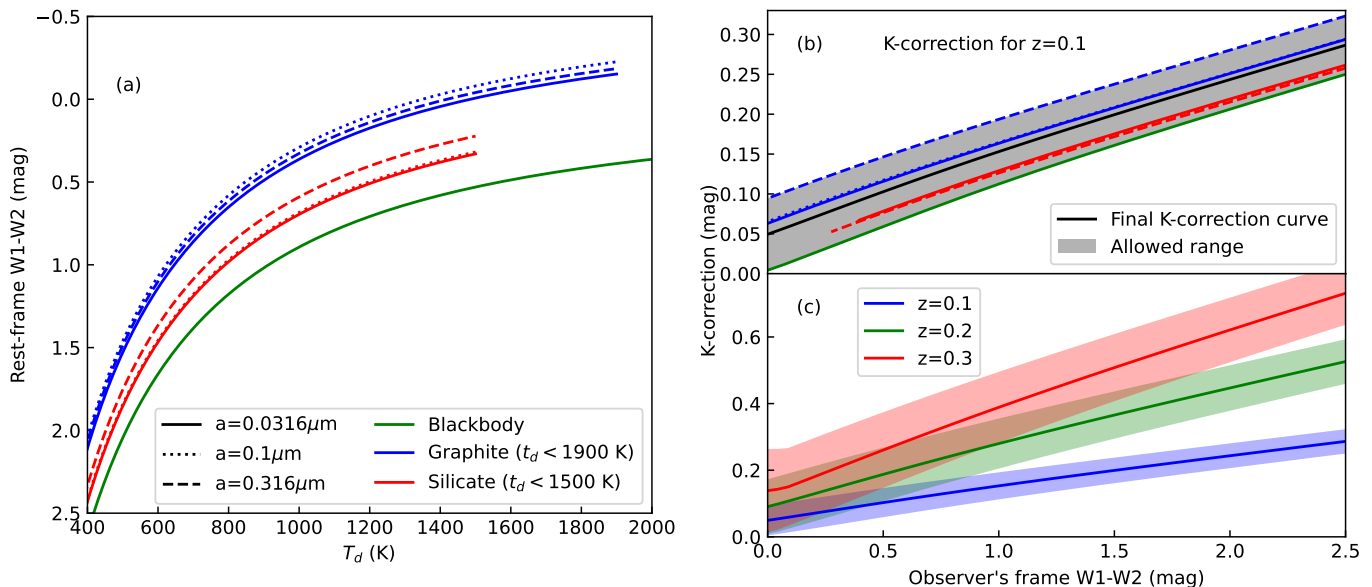


Figure B1. (a): Rest-frame $W1 - W2$ color as functions of temperature for different types of SEDs. Blue, red and green lines represent results of optically thin graphite and silicate dust, and blackbody. For graphite and silicate dust, results assuming grain radii of 0.0316, 0.1 and 0.316 μm are shown using solid, dotted and dashed lines. (b): The K-correction for $z = 0.1$ as functions of color in the observer's frame for different types of SEDs. The meanings of colors and styles of the lines are the same as panel (a). The grey shades show the allowed range of K-correction, and the black solid line shows the final K-correction curve. (c): The final K-correction curves and allowed range for $z = 0.1, 0.2$ and 0.3 .

systematic errors both increase as z increases, as shown in Figure B1(c). The systematic error caused by uncertain types of SEDs can be roughly estimated as $\sigma_{\text{sys}}(K) \approx 0.04z$.

C. ANALYSIS OF THE 2020 OUTBURST OF MRK 1018

Mrk1018 is a famous CLAGN. It changed from type 1.9 to type 1 between 1979 and 1984 (Cohen et al. 1986), and back to type 1.9 between 2010 and 2015 (Husemann et al. 2016). In 2020, it changed to type 1 again, along with a giant outburst lasting for about one year, and then returned to type 1.9 after the outburst ended.

In this work, we are only concerned with the shape of the UV LC of the 2020 outburst. Does it rise quickly and fall slowly like ANT, or does it have a similar rise time and fall time like most CLAGNs? This is hard to answer because Mrk 1018 has no observations from March to June 2020, which is the expected rise phase. Lu et al. (2025) found that the optical LCs can be fitted equally well with two models: one is a Gaussian model, and the other is a GE model including a Gaussian rise and an exponential fall. In the GE model, the rise and fall times can be represented by σ and τ , respectively. Thus, comparing σ and τ tells one what type of LC it is. Using ZTF and ATLAS LCs, Lu et al. (2025) yielded best-fitting parameters of $\sigma \sim 90 - 110$ days and $\tau \sim 60 - 80$ days, and therefore, they concluded that the outburst has similar rise time and fall time.

We refit the same data using the GE model. We reduced the ZTF and ATLAS data and generated host-subtracted LCs following Wang et al. (2024). We fit the data simultaneously instead of fitting ZTF and ATLAS data separately as Lu et al. (2025) did. We fit by the Monte-Carlo Markov-Chain (MCMC) method with the code *emcee* assuming log-uniformly prior distributions for σ and τ . The posterior probability density distributions of σ and τ are displayed in Figure C1(a). As can be seen from the figure, the observed data can be reproduced by two different groups of parameters, which can roughly be divided by the threshold of $\sigma = 60$ day. For one group $\sigma = 33 \pm 14$ day and $\tau = 116 \pm 6$ day, representing fast rising models with shorter rise time than fall time (Figure C1(b)). And for the other group $\sigma = 98^{+8}_{-11}$ day and $\tau = 83^{+14}_{-10}$ day, representing slowly rising models with similar rise time and fall time (Figure C1(c)). The integral posterior probabilities for the two groups are 17% and 83%, respectively, indicating that slowly rising models have a higher probability, but fast-rising models are also acceptable by the data. Taking into account systematic errors due to AGN intrinsic variability, the differences between the two groups of models would be even smaller. Therefore, we concluded that the LC data alone cannot rule out the possibility of UV LCs with fast rise and slow fall.

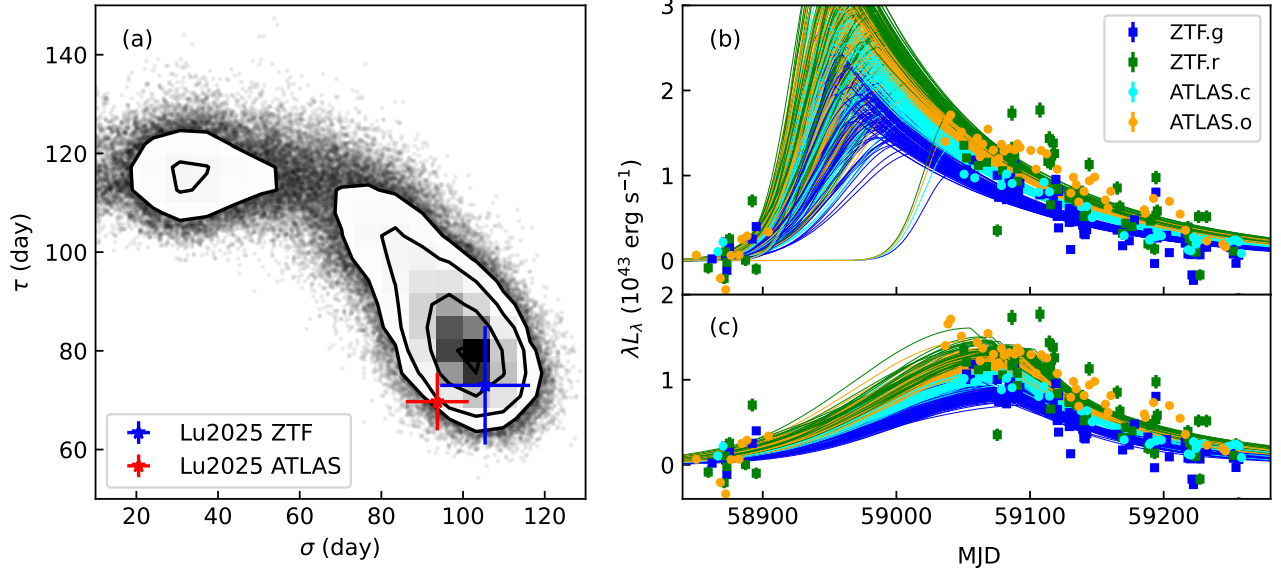


Figure C1. (a): Posterior probability density distributions of σ and τ of the GP model. We show the parameters derived from ZTF (blue) and ALTAS (red) data separately by Lu et al. (2025) with stars for comparison. These parameters are consistent with our slowly rising models with higher probability, confirming that the GE models of Lu et al. (2025) are best-fitting. However, they ignored fast-rising models, which are also acceptable. (b): Fast rising models ($\sigma < 60$ days) in the ZTF/g (blue), ZTF/r (green), ATLAS/c (cyan) and ATLAS/o (orange) bands and the observed data. We show 100 randomly selected MCMC realizations. (c): Same as (b) but show slowly rising models ($\sigma > 60$ days).

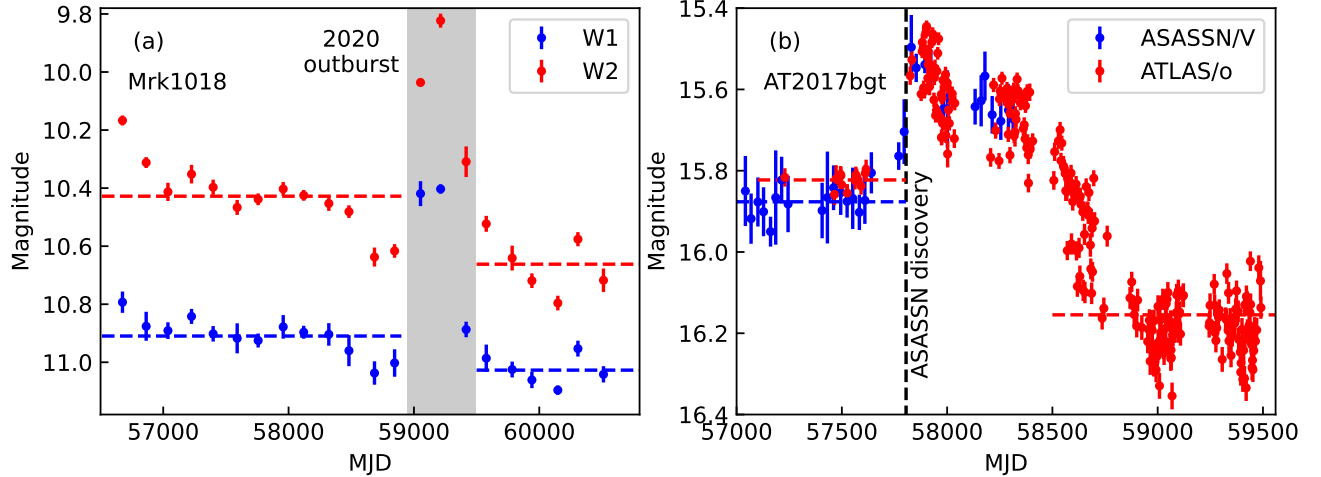


Figure C2. (a): WISE MIR LC of Mrk 1018, and the levels before and after the 2020 outburst in dashed lines in W1 (blue) and W2 (red) bands. (b): ASASSN/V and ATLAS/o LCs of AT 2017bgt. We labeled the discovery time of the flare and the levels before and after the flare.

A rapid outburst occurred during a long-term turning-off changing-look event in Mrk 1018. As such rapid outbursts are rare, the outburst and the changing-look event are likely physically related (Lu et al. 2025). Here, we present a similar case AT 2017bgt, an outburst in a type 1 AGN (Trakhtenbrot et al. 2019). As shown in Figure C2, after the outburst, the optical flux dropped to a lower level than before the outburst, suggesting an underlying long-term dimming trend of the AGN, similar to Mrk 1018. This similarity may imply a similar physical origin; hence, the outburst in Mrk 1018 may have similar properties to AT 2017bgt. Thus, for our study of color variation of the MIR outbursts, it is uncertain whether Mrk 1018 should be classified as CLAGN or ANT.

D. THE PARAMETERS OF MIR COLOR VARIATION FOR THE MIR SELECTED SAMPLES

This section lists the CVR, IC and probabilities of falling into U, M and L regions. The parameters of the MIRONGs hosted in non-Seyfert and Seyfert galaxies are listed in Table D1 and Table D2, respectively, and those of the WTP sample are listed in Table D3.

Table D1. CVR and IC of the MIRONGs in non-Seyfert galaxies.

Object	Redshift	subsample	CVR	IC	p_U	p_M	p_L
SDSS J0045-0047	0.05677	Star-forming	0.04 ± 0.22	0.93 ± 0.31	4.85%	34.35%	60.80%
SDSS J0103+1401	0.04181	Star-forming	-0.07 ± 0.03	1.04 ± 0.02	0.00%	0.00%	100.00%
SDSS J0121+1405	0.12938	Star-forming	0.43 ± 0.66	0.75 ± 0.23	51.58%	17.27%	31.16%
SDSS J0205+0004	0.07649	Star-forming	0.31 ± 0.11	0.71 ± 0.04	20.89%	76.80%	2.31%
SDSS J0757+1908	0.10501	Composite	0.33 ± 0.23	0.48 ± 0.32	38.26%	45.42%	16.32%
SDSS J0814+2611	0.07567	Star-forming	0.54 ± 0.41	0.78 ± 0.32	62.98%	22.58%	14.45%
SDSS J0837+4143	0.09806	Composite	1.45 ± 0.80	0.54 ± 0.29	90.63%	4.81%	4.56%
SDSS J0847+5142	0.11997	Star-forming	0.36 ± 1.05	1.20 ± 0.29	48.32%	11.52%	40.17%
SDSS J0859+0922	0.15188	Star-forming	0.07 ± 0.06	0.59 ± 0.08	0.00%	32.89%	67.11%
SDSS J0909+1920	0.10716	Composite	0.21 ± 0.14	0.89 ± 0.10	9.33%	69.00%	21.68%
SDSS J0915+4814	0.10049	LINER	0.12 ± 0.27	0.56 ± 0.39	14.06%	38.04%	47.90%
SDSS J0931+6626	0.08729	LINER	-0.05 ± 0.28	1.06 ± 0.35	4.83%	24.04%	71.13%
SDSS J0943+5958	0.07491	LINER	0.27 ± 0.83	1.23 ± 0.24	43.94%	14.16%	41.90%
SDSS J0944+3105	0.03465	Composite	0.28 ± 0.22	0.79 ± 0.19	29.17%	49.85%	20.98%
SDSS J0957+0207	0.12528	Composite	0.54 ± 0.54	0.56 ± 0.24	59.47%	19.19%	21.34%
SDSS J1001+1829	0.10603	Star-forming	0.44 ± 0.52	0.59 ± 0.19	52.00%	21.75%	26.25%
SDSS J1002+4424	0.15446	LINER	-0.10 ± 0.70	1.60 ± 0.25	23.95%	15.02%	61.03%
SDSS J1011+5348	0.2344	LINER	0.22 ± 0.14	0.24 ± 0.25	8.64%	71.01%	20.35%
SDSS J1020+2515	0.13145	Star-forming	0.73 ± 0.91	0.60 ± 0.32	63.75%	11.48%	24.77%
SDSS J1037+3912	0.10677	Star-forming	0.31 ± 0.18	0.94 ± 0.12	30.76%	56.00%	13.24%
SDSS J1043+2716	0.12812	Composite	0.04 ± 0.09	0.73 ± 0.16	0.00%	25.14%	74.86%
SDSS J1053+5524	0.15174	Star-forming	1.20 ± 0.74	0.94 ± 0.17	85.49%	7.34%	7.17%
SDSS J1058+5444	0.13062	Star-forming	0.54 ± 0.48	0.88 ± 0.19	61.42%	20.53%	18.05%
SDSS J1109+3708	0.02602	LINER	0.08 ± 0.12	0.81 ± 0.20	0.41%	44.02%	55.57%
SDSS J1111+5923	0.16973	Composite	0.51 ± 0.45	0.50 ± 0.13	59.48%	22.11%	18.41%
SDSS J1115+0544	0.08995	LINER	0.41 ± 0.08	0.68 ± 0.06	54.83%	45.16%	0.01%
SDSS J1120+1933	0.1278	Composite	0.62 ± 0.45	0.34 ± 0.21	69.23%	18.73%	12.04%
SDSS J1124+0455	0.07398	Composite	-0.04 ± 0.20	1.41 ± 0.15	1.70%	23.59%	74.71%
SDSS J1129+5131	0.03286	Composite	0.38 ± 0.70	1.53 ± 0.23	48.88%	16.67%	34.45%
SDSS J1139+6134	0.13461	Star-forming	0.07 ± 0.15	0.96 ± 0.27	1.37%	41.38%	57.25%
SDSS J1152+4850	0.15102	Composite	-0.08 ± 0.12	0.83 ± 0.25	0.01%	6.96%	93.03%
SDSS J1153+4037	0.1451	Star-forming	-0.02 ± 0.26	0.79 ± 0.11	5.57%	27.27%	67.15%
SDSS J1203+5859	0.04692	Star-forming	0.26 ± 0.44	1.02 ± 0.15	37.46%	26.29%	36.26%
SDSS J1218+2951	0.13559	Composite	0.14 ± 0.07	0.79 ± 0.15	0.01%	69.54%	30.45%
SDSS J1219+0516	0.08251	Composite	0.11 ± 0.17	0.66 ± 0.25	3.83%	47.76%	48.42%
SDSS J1242+2537	0.08789	Composite	0.15 ± 0.48	0.79 ± 0.23	29.70%	23.66%	46.64%
SDSS J1245-0147	0.21543	LINER	0.48 ± 0.44	0.61 ± 0.15	57.46%	23.35%	19.19%
SDSS J1305+3953	0.07249	LINER	0.57 ± 0.34	0.61 ± 0.13	69.45%	22.48%	8.07%
SDSS J1310+2518	0.16039	Composite	0.34 ± 0.31	0.37 ± 0.25	42.75%	35.47%	21.78%
SDSS J1322+3301	0.1269	LINER	-0.21 ± 0.64	0.92 ± 0.23	16.50%	14.30%	69.20%
SDSS J1329+2341	0.07171	Composite	0.24 ± 0.11	0.98 ± 0.16	7.99%	81.20%	10.82%
SDSS J1341-0049	0.17538	Composite	0.41 ± 0.36	0.17 ± 0.29	50.24%	29.49%	20.27%

Table D1. CVR and IC of the MIRONGs in non-Seyfert galaxies.

Object	Redshift	subsample	CVR	IC	p_U	p_M	p_L
SDSS J1352+0009	0.16596	LINER	0.42 ± 0.40	0.32 ± 0.25	52.59%	26.29%	21.12%
SDSS J1409+1057	0.05972	LINER	0.93 ± 0.65	0.35 ± 0.24	79.56%	10.46%	9.98%
SDSS J1412+4114	0.1025	Composite	-0.27 ± 0.58	0.87 ± 0.19	12.61%	13.75%	73.64%
SDSS J1422+0609	0.05636	Composite	0.28 ± 0.10	0.28 ± 0.23	12.17%	83.49%	4.34%
SDSS J1424+6249	0.10913	Composite	0.19 ± 0.11	0.55 ± 0.14	3.76%	75.45%	20.79%
SDSS J1440+1758	0.11574	Composite	0.29 ± 0.59	0.58 ± 0.18	42.85%	19.70%	37.45%
SDSS J1442+5558	0.07689	Composite	0.00 ± 0.12	0.62 ± 0.26	0.04%	19.38%	80.58%
SDSS J1447+4023	0.13025	LINER	0.49 ± 0.14	0.37 ± 0.05	73.95%	25.82%	0.22%
SDSS J1448+1137	0.06657	Star-forming	-0.15 ± 0.43	1.15 ± 0.38	9.40%	17.88%	72.72%
SDSS J1508+2602	0.08255	Composite	0.18 ± 0.26	1.26 ± 0.18	19.60%	42.15%	38.26%
SDSS J1512+2809	0.11552	LINER	0.23 ± 0.25	0.86 ± 0.15	25.70%	43.96%	30.34%
SDSS J1513+3111	0.07181	Composite	0.65 ± 0.22	0.45 ± 0.10	86.13%	13.05%	0.82%
SDSS J1524+5314	0.08513	Star-forming	0.54 ± 0.26	0.36 ± 0.09	70.91%	24.79%	4.30%
SDSS J1541+0718	0.16305	Star-forming	0.20 ± 0.17	0.80 ± 0.28	13.25%	59.63%	27.12%
SDSS J1548+2208	0.03127	Composite	-0.08 ± 0.03	1.09 ± 0.07	0.00%	0.00%	100.00%
SDSS J1554+3629	0.23683	Composite	0.11 ± 0.14	0.39 ± 0.23	1.95%	50.25%	47.80%
SDSS J1555+2120	0.07094	Composite	0.05 ± 0.09	0.94 ± 0.20	0.01%	30.16%	69.83%
SDSS J1600+4612	0.19742	Star-forming	0.51 ± 0.46	0.69 ± 0.13	59.50%	21.89%	18.60%
SDSS J1612+1416	0.072	Composite	0.08 ± 0.19	1.02 ± 0.33	4.48%	40.30%	55.23%
SDSS J1628+4810	0.12454	Star-forming	1.14 ± 0.80	0.69 ± 0.27	82.26%	8.09%	9.65%
SDSS J1632+4416	0.05789	LINER	0.24 ± 0.27	0.76 ± 0.11	26.41%	41.95%	31.64%
SDSS J1647+3843	0.08547	Star-forming	0.27 ± 0.07	0.64 ± 0.05	3.43%	95.58%	0.98%
SDSS J2146+1041	0.16358	Star-forming	0.54 ± 0.46	0.29 ± 0.18	61.14%	20.93%	17.93%
SDSS J2203+1124	0.18627	Composite	0.18 ± 0.13	0.45 ± 0.25	4.11%	70.85%	25.04%
SDSS J2215-0107	0.04775	Composite	0.25 ± 0.19	0.60 ± 0.35	21.84%	57.34%	20.81%
SDSS J2312+1335	0.16553	Composite	0.55 ± 0.51	0.59 ± 0.18	61.69%	19.49%	18.83%

E. SIMULATIONS OF DUST ECHOES

In this section, we described the simulations we made which are not present in the main text. In subsequent simulations, we will focus on the two cases: a TDE case with TDE form UV LCs and no underlying AGN, and a CLAGN case with LINEAR form UV LCs and underlying AGN with L_{AGN} the same as the peak luminosity L_{max} .

E.1. Influence by peak UV luminosity and duration

We studied the influence of different UV peak luminosities L_{max} in the range of $10^{43} - 10^{45}$ erg s $^{-1}$ (Figure E1(a), (b)). For both the TDE and CLAGN cases, CVR in the rising phases decreases with the increase of L_{max} , while IC is little affected.

According to the literature, the peak UV luminosities of MIR bright TDEs are between $10^{43.4}$ and $10^{45.7}$ erg s $^{-1}$ (Onori et al. 2022; Wang et al. 2024; Yao et al. 2023; Earl et al. 2024; Zhang et al. 2025). CLAGNs' peak UV luminosities range widely. Assuming that L_{UV} is ~ 10 times L_{W2} according to typical AGNs' SEDs, the CLAGN sample in this work have peak UV luminosities in the range of $\sim 10^{43} - 10^{45}$ erg s $^{-1}$. There is no significant overall difference in the peak UV luminosities of the TDE and CLAGN samples. Thus, it can hardly explain the observed difference between TDEs and CLAGNs with the difference in peak UV luminosities. However, the dispersion of peak UV luminosities may explain the internal CVR dispersion among TDEs, ANTs or CLAGNs.

We then studied the influence of different durations τ in the range of $10^6 - 10^8$ s (Figure E1(c), (d)). For the TDE case, CVR in the rising phase decreases with the increase of τ . When τ increases to $\sim 10^{7.5} - 10^8$ s ($\sim 1 - 3$ years), the CVR drops to values similar to those in CLAGNs. Fortunately, the durations of most TDEs and ANTs are not that long, and thus the results obtained by assuming $\tau = 10^7$ s are not affected. While for the CLAGN form, CVR is little affected by τ .

Table D2. CVR and IC of the MIRONGs in Seyfert galaxies.

Object	Redshift	CVR	IC	p_U	p_M	p_L
SDSS J0000+1438	0.1366	0.30 ± 0.21	0.52 ± 0.25	31.86%	51.02%	17.11%
SDSS J0027+0713	0.13109	0.29 ± 0.48	0.65 ± 0.38	41.01%	24.30%	34.69%
SDSS J0158-0052	0.08044	0.36 ± 0.06	0.28 ± 0.14	26.68%	73.32%	0.00%
SDSS J0745+2655	0.11481	0.08 ± 0.30	0.89 ± 0.11	14.76%	33.47%	51.77%
SDSS J0811+4054	0.06704	0.04 ± 0.43	0.70 ± 0.17	20.38%	24.02%	55.60%
SDSS J0841+0526	0.15631	0.27 ± 0.12	0.64 ± 0.12	14.79%	76.34%	8.87%
SDSS J0854+1113	0.16719	0.07 ± 0.35	0.48 ± 0.30	17.26%	29.41%	53.33%
SDSS J1003+0202	0.1247	0.45 ± 0.33	0.48 ± 0.10	55.48%	29.56%	14.96%
SDSS J1008+1549	0.11765	0.07 ± 0.15	0.24 ± 0.22	1.35%	40.54%	58.11%
SDSS J1009+3436	0.20863	-0.18 ± 0.58	0.91 ± 0.25	16.75%	15.59%	67.66%
SDSS J1017+1224	0.10762	0.28 ± 0.37	0.72 ± 0.10	38.71%	30.70%	30.59%
SDSS J1041+3412	0.14028	-0.20 ± 0.81	0.59 ± 0.30	23.82%	12.73%	63.44%
SDSS J1051+2101	0.06593	-0.42 ± 0.61	1.07 ± 0.19	9.05%	10.80%	80.14%
SDSS J1105+5941	0.03369	0.11 ± 0.05	0.62 ± 0.11	0.00%	54.86%	45.14%
SDSS J1114+4056	0.15247	0.28 ± 0.19	0.31 ± 0.34	26.14%	56.90%	16.96%
SDSS J1133+6701	0.03968	0.13 ± 0.06	0.47 ± 0.09	0.00%	66.58%	33.42%
SDSS J1200+0648	0.03599	0.04 ± 0.16	1.24 ± 0.36	1.40%	33.82%	64.79%
SDSS J1201+3525	0.19031	0.16 ± 0.21	0.50 ± 0.38	13.08%	47.86%	39.06%
SDSS J1208+3305	0.28028	-0.02 ± 0.27	0.71 ± 0.31	5.52%	26.73%	67.75%
SDSS J1238+0815	0.11378	0.09 ± 0.13	0.70 ± 0.26	0.85%	44.57%	54.58%
SDSS J1308+0429	0.04832	-0.93 ± 0.53	1.37 ± 0.25	0.60%	1.98%	97.42%
SDSS J1332+2036	0.11249	1.00 ± 0.12	0.43 ± 0.05	100.00%	0.00%	0.00%
SDSS J1340+1842	0.09018	0.12 ± 0.22	0.75 ± 0.25	9.58%	43.62%	46.80%
SDSS J1341+1516	0.12553	0.21 ± 0.27	0.78 ± 0.21	23.89%	42.39%	33.72%
SDSS J1402+3922	0.06375	1.08 ± 0.18	0.21 ± 0.08	99.99%	0.01%	0.00%
SDSS J1430+2303	0.08105	0.01 ± 0.12	0.68 ± 0.24	0.04%	22.56%	77.40%
SDSS J1504+0107	0.12826	0.14 ± 0.16	0.52 ± 0.33	5.00%	54.47%	40.53%
SDSS J1511+2214	0.12048	-0.01 ± 0.27	0.78 ± 0.20	6.51%	27.49%	66.00%
SDSS J1533+2729	0.07193	-0.18 ± 0.21	0.85 ± 0.18	0.32%	8.90%	90.77%
SDSS J1537+5814	0.09356	0.10 ± 0.16	0.44 ± 0.22	2.97%	47.90%	49.12%
SDSS J1556+4513	0.1808	0.22 ± 0.17	0.52 ± 0.12	14.28%	61.72%	24.00%
SDSS J1657+2345	0.05914	0.13 ± 0.02	0.79 ± 0.04	0.00%	94.32%	5.68%
SDSS J1659+2049	0.04513	0.51 ± 0.58	0.96 ± 0.22	57.64%	18.75%	23.62%
SDSS J2115-0011	0.23285	0.55 ± 0.70	0.29 ± 0.21	58.56%	15.59%	25.85%
SDSS J2141-0857	0.08729	0.21 ± 0.17	0.89 ± 0.20	12.77%	60.16%	27.07%
SDSS J2150-0106	0.08791	0.29 ± 0.05	0.35 ± 0.06	2.23%	97.76%	0.01%
SDSS J2156+0041	0.05389	0.44 ± 0.64	1.18 ± 0.26	52.74%	17.75%	29.51%
SDSS J2310+2220	0.07829	-0.37 ± 0.81	1.03 ± 0.29	17.11%	11.04%	71.85%

E.2. Influence by shape of dust structure

We first studied the influence of the initial inner radius r_{in} on CVR and IC (Figure E2(a), (b)). We tried three r_{in} values of 0.03, 0.1 and 0.3 pc, which are 0.24, 0.8 and 2.4 times r_{sub} ($= 0.13$ pc for $L_{\text{max}} = 10^{44}$ erg s $^{-1}$), respectively. The results show that r_{in} has little effect on the MIR color variation when it is much smaller than r_{sub} . However, when r_{in} is close to or greater than r_{sub} , the increase of r_{in} leads to the increase of IC for both TDE and CLAGN cases, and leads to the decrease of CVR for the TDE case.

Table D3. CVR and IC of the WTP sample.

Object	Redshift	subsample	CVR	IC	p_U	p_M	p_L
WTP14abnpgk	0.02035	Silver	0.14 ± 0.22	0.81 ± 0.18	11.87%	44.56%	43.57%
WTP14acnjbu	0.026	Silver	0.12 ± 0.17	1.20 ± 0.15	5.64%	49.81%	44.55%
WTP14adbwvs	0.02489	Silver	0.23 ± 0.24	1.33 ± 0.18	23.62%	45.99%	30.39%
WTP14adeqka	0.01895	Gold	0.11 ± 0.10	1.04 ± 0.23	0.14%	52.66%	47.20%
WTP15abyndq	0.03742	Gold	0.19 ± 0.22	0.21 ± 0.34	16.94%	49.27%	33.80%
WTP15acbgpn	0.03369	Silver	0.11 ± 0.05	0.61 ± 0.11	0.00%	56.31%	43.69%
WTP16aatsnw	0.04513	Silver	0.54 ± 0.57	0.95 ± 0.22	59.84%	18.28%	21.88%
WTP17aalddb	0.04832	Gold	-0.92 ± 0.52	1.36 ± 0.25	0.59%	2.02%	97.39%
WTP17aalzpx	0.03725	Gold	0.17 ± 0.18	0.77 ± 0.26	9.61%	56.06%	34.34%
WTP17aamoxe	0.042	Gold	0.88 ± 0.07	0.45 ± 0.03	100.00%	0.00%	0.00%
WTP17aamzew	0.03465	Gold	0.28 ± 0.22	0.78 ± 0.19	29.44%	49.94%	20.63%
WTP17aanbso	0.04692	Gold	0.30 ± 0.45	1.01 ± 0.15	41.46%	25.82%	32.73%
WTP18aajkmk	0.0287	Gold	0.08 ± 0.05	0.57 ± 0.04	0.00%	39.22%	60.78%
WTP18aamced	0.03672	Silver	1.09 ± 0.62	0.35 ± 0.32	86.50%	7.86%	5.64%
WTP18aampwj	0.0375	Gold	0.32 ± 0.04	0.51 ± 0.05	1.56%	98.45%	0.00%

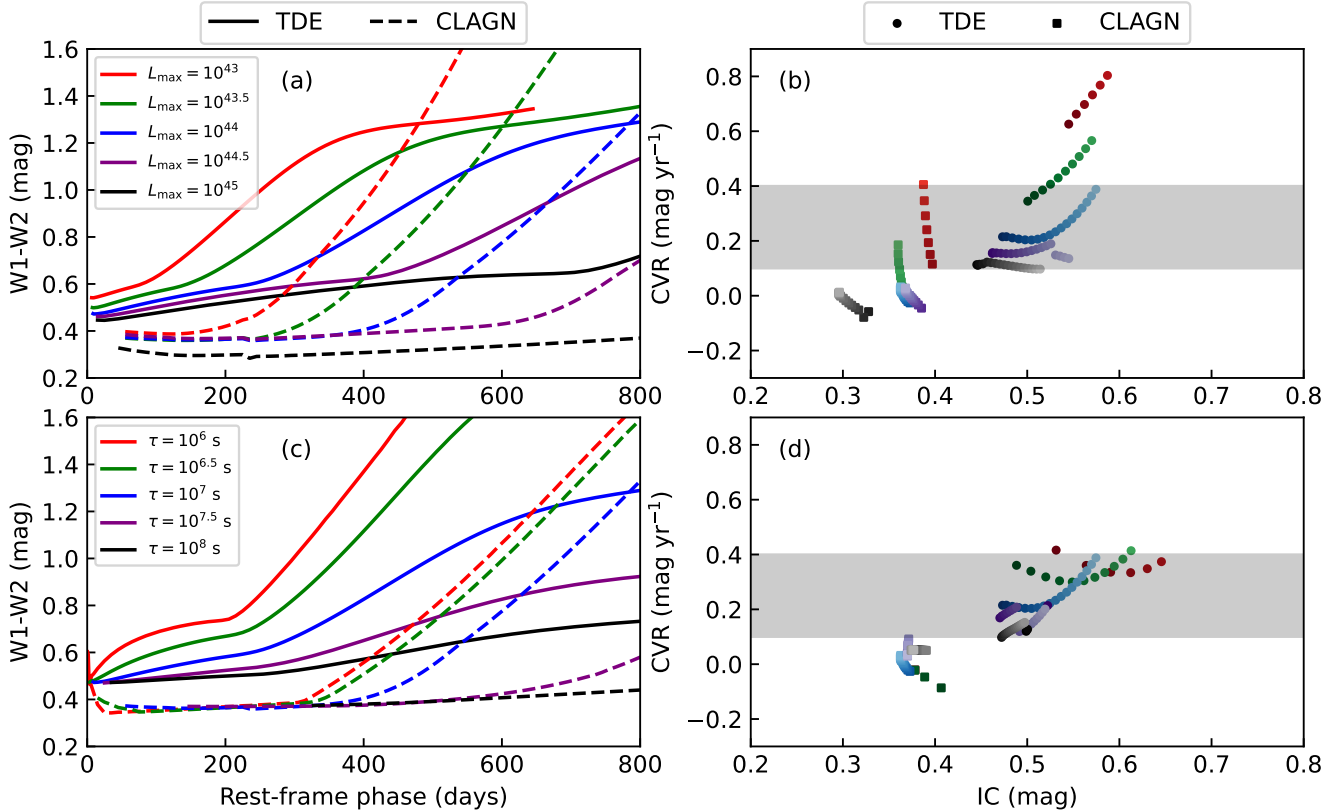


Figure E1. Simulations exploring the influence by peak UV luminosity L_{\max} and duration τ . Panels (a) and (c) show the MIR color curves (solid and dashed for the TDE and CLAGN cases, respectively), and (b) and (d) show the inferred ICs and CVRs using the sampled data (circles and squares for the TDE and CLAGN cases, respectively). Different colors indicate different L_{\max} for panels (a) and (b), and indicate different τ for panels (c) and (d).

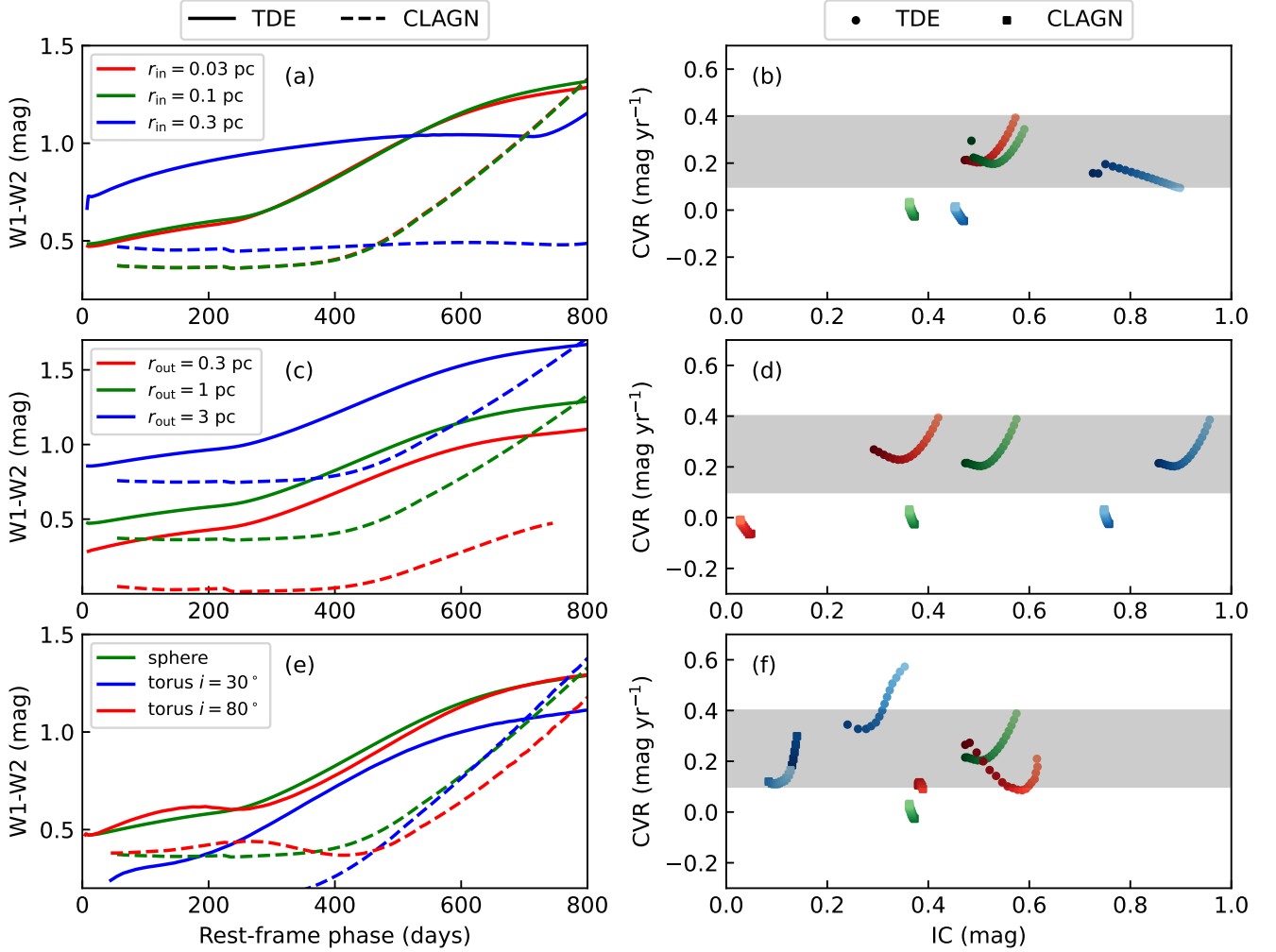


Figure E2. Simulations exploring the influence of the shape of dust structure. Panels (a), (c) and (e) show the MIR color curves (solid and dashed for the TDE and CLAGN cases, respectively), and (b), (d) and (f) show the inferred ICs and CVRs using the sampled data (circles and squares for the TDE and CLAGN cases, respectively). Different colors indicate different r_{in} for panels (a) and (b), and different r_{out} for panels (c) and (d), and different geometries for panels (e) and (f).

We then studied the influence of the outer radius r_{out} in the range of 0.3–3 pc (Figure E2(c), (d)). The r_{out} has little effect on CVR, but significantly affects IC. This is because the IR emission in the rising phase mainly comes from the inner region of the dust structure, and the outer region only affects the optical depth of the emergent IR emission. Therefore, the difference in r_{out} cannot explain the difference in CVRs, but can explain the differences and dispersions of ICs. In our simulations, we fixed grain radius a_0 at $0.1 \mu\text{m}$ and number density n_d at 10^8 cm^{-3} . The actual quantity directly related to IC is the radial optical depth of the dust shell, which can be described by the dimensionless parameter $\tau_{\text{dust}} = (r_{\text{out}} - r_{\text{sub}})\pi a_0^2 n_d$.

We finally studied the influence of different dust geometries between active (torus) and inactive galaxies (roughly isotropic). We further developed the radiative transfer model so that it can calculate the echo of a torus. The torus is described by a half-opening angle and an inclination of i between the axis of the torus and the line of sight. We set the half-opening angle to be 50° , and considered two inclinations, 30° for face-on torus and 80° for edge-on torus.

The results are shown in Figure E2(e), (f). The edge-on torus leads to close IC and CVR compared with spherical shell, while face-on torus dust leads to much smaller IC and slightly larger CVR than spherical shell and edge-on torus. The reason for the much smaller IC for face-on torus is that the initial MIR emission, mainly from the inner region of the dust structure, emerges with a much smaller optical depth. The effect would be more pronounced when the dust shell is thicker. In addition, the reason for the slightly larger CVR may be that the echo produced by the peak

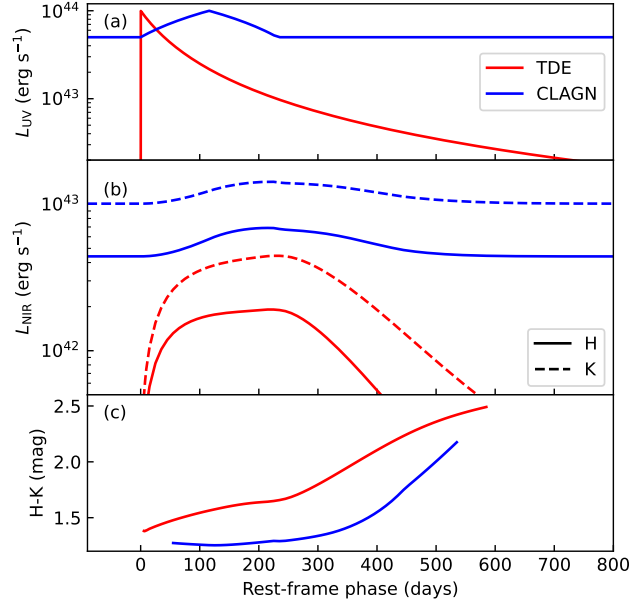


Figure E3. (a): The assumed UV LCs for TDE and CLAGN cases. (b): The simulated NIR LCs in the H (solid) and K (dashed) bands. (c): The inferred H-K color curves.

luminosity is bluer due to smaller emergent optical depth, and has a larger color difference with the echo produced by the long tail and outer region with redder color.

Our radiative transfer model assumes uniform dust, but it is possible that the actual AGN dusty torus is clumpy (Nenkova et al. 2008). Assuming clumpy dust, it can also be deduced that the IR emission from the inner region of face-on torus has a smaller emergent optical depth than those of spherical shell and edge-on torus. Therefore, the above conclusions about IC hold, regardless whether the dust is uniform or clumpy.

E.3. Prediction on variation of NIR color

We studied the possible difference in the NIR color of TDEs and CLAGNs using simulations. For the TDE case, we set an outburst with TDE form UV LC with $L_{\max} = 10^{44}$ erg s^{-1} . While for the CLAGN case, we set an outburst with LINEAR form UV LC with $L_{\max} = 5 \times 10^{43}$ erg s^{-1} and an underlying AGN with $L_{\text{AGN}} = 5 \times 10^{43}$ erg s^{-1} . The settings of other parameters were the same as in subsection 4.1.1. We calculated the NIR LCs in H and K bands and the variation of $H - K$ color. As shown in Figure E3, the NIR color of TDEs turns red rapidly in the rising phase, while that of CLAGNs keeps nearly steady in the rising phase. Our simulations suggest that the NIR color variation has the potential to distinguish TDEs from CLAGNs.